



1 **Defining BGC-Argo-based metrics of ocean health and biogeochemical**  
2 **functioning for the evaluation of global ocean models**

3

4

5 Alexandre Mignot<sup>1</sup>, Hervé Claustre<sup>2,3</sup>, Gianpiero Cossarini<sup>4</sup>, Fabrizio D’Ortenzio<sup>2,3</sup>, Elodie  
6 Gutknecht<sup>1</sup>, Julien Lamouroux<sup>1</sup>, Paolo Lazzari<sup>4</sup>, Coralie Perruche<sup>1</sup>, Stefano Salon<sup>4</sup>, Raphaëlle  
7 Sauzède<sup>3</sup>, Vincent Taillandier<sup>2,3</sup>, Anna Teruzzi<sup>4</sup>

8

9 <sup>1</sup>Mercator Océan International, Ramonville-Saint-Agne, France

10 <sup>2</sup>Laboratoire d’Océanographie de Villefranche-sur-Mer, Villefranche-sur-Mer, CNRS and  
11 Sorbonne Université, 06230 Villefranche-sur-Mer, France

12 <sup>3</sup>Institut de la Mer de Villefranche, CNRS and Sorbonne Université, 06230 Villefranche-sur-  
13 Mer, France

14 <sup>4</sup>National Institute of Oceanography and Applied Science-OGS, Trieste, Italy

15

16

17 Numerical models of ocean biogeochemistry are becoming a major tool to detect and  
18 predict the impact of climate change on marine resources and ocean health. Classically, the  
19 validation of such models relies on comparison with surface quantities from satellite (such as  
20 chlorophyll-*a* concentrations), climatologies, or sparse *in situ* data (such as cruises  
21 observations, and permanent fixed oceanic stations). However, these datasets are not fully  
22 suitable to assess how models represent many climate-relevant biogeochemical  
23 processes. These limitations now begin to be overcome with the availability of a large  
24 number of vertical profiles of light, pH, oxygen, nitrate, chlorophyll-*a* concentrations and  
25 particulate backscattering acquired by the Biogeochemical-Argo (BGC-Argo) floats network.  
26 Additionally, other key biogeochemical variables such as dissolved inorganic carbon and  
27 alkalinity, not measured by floats, can be predicted by machine learning-based methods  
28 applied to float oxygen concentrations. Here, we demonstrate the use of the global array of  
29 BGC-Argo floats for the validation of biogeochemical models at the global scale. We first  
30 present 18 key metrics of ocean health and biogeochemical functioning to quantify the  
31 success of BGC model simulations. These metrics are associated with the air-sea CO<sub>2</sub> flux,  
32 the biological carbon pump, oceanic pH, oxygen levels and Oxygen Minimum Zones



1 (OMZs). The metrics are either a depth-averaged quantity or correspond to the depth of a  
2 particular feature. We also suggest four diagnostic plots for displaying such metrics.

### 4 **1. Introduction**

5  
6 Since pre-industrial times, the ocean had taken up ~36 % of the CO<sub>2</sub> emitted by the  
7 combustion of fossil fuel (Friedlingstein et al., 2019) leading to dramatic change in the  
8 ocean's biogeochemical (BGC) cycles, such as ocean acidification (Iida et al., 2020).  
9 Moreover, deoxygenation (Breitburg et al., 2018) and change in the biological carbon pump  
10 are now manifesting on a global scale (Capuzzo et al., 2018; Osman et al., 2019; Roxy et al.,  
11 2016). Together with plastic pollution (Eriksen et al., 2014) and an increase in fisheries  
12 pressure (Crowder et al., 2008), major changes are therefore occurring in marine ecosystems  
13 at the global scale. In order to monitor these ongoing changes, derive climate projections and  
14 develop better mitigation strategies, realistic numerical simulations of the oceans' BGC state  
15 are required.

16  
17 Numerical models of ocean biogeochemistry represent a prime tool to address these issues  
18 because they produce three dimensional estimates of a large number of chemical and  
19 biological variables that are dynamically consistent with the ocean circulation (Fennel et al.,  
20 2019). They can assess past and current states of the biogeochemical ocean, produce short-  
21 term to seasonal forecasts as well as climate projections. However, these models are far from  
22 being flawless, mostly because there are still huge knowledge gaps in the understanding of  
23 key biogeochemical processes and, as a result, the mathematical functions that describe BGC  
24 fluxes and ecosystems dynamics are too simplistic (Schartau et al., 2017). For instance, most  
25 models do not include a radiative component for the penetration of solar radiation in the  
26 ocean. It has been nevertheless shown that coupling such a component with a BGC model  
27 improves the representation of the dynamics of phytoplankton in the lower euphotic zone  
28 (Dutkiewicz et al., 2015). Additionally, the parameterisation of the mathematical functions  
29 generally result from laboratory experiments on few a priori expected representative species  
30 and may not be suitable for extrapolation to ocean simulations that need to represent the large  
31 range of organisms present in oceanic ecosystems (Schartau et al., 2017; Ward et al., 2010).  
32 Furthermore, the assimilation of physical data in coupled physical-BGC models that improves  
33 the physical ocean state can paradoxically degrade the simulation of the BGC state of the



1 ocean (Fennel et al., 2019; Park et al., 2018). A rigorous validation of BGC models is thus  
2 essential to test their predictive skills, their ability to reproduce BGC processes and estimate  
3 confidence intervals on model predictions (Doney et al., 2009; Stow et al., 2009).

4  
5 However, the validation of BGC models is presently limited by the availability of data. It  
6 relies principally on comparison with surface quantities from satellite (such as chlorophyll-*a*  
7 concentrations), cruises observations, and few permanent oceanic stations (e.g., Doney et al.,  
8 2009; Dutkiewicz et al., 2015; Lazzari et al., 2012, 2016; Lynch et al., 2009; Séférian et al.,  
9 2013; Stow et al., 2009). All these datasets neither have a sufficient vertical or temporal  
10 resolution, nor a synoptic view nor can provide all variables necessary to evaluate how  
11 models represent climate-relevant processes such as the air-sea CO<sub>2</sub> fluxes, the biological  
12 carbon pump, ocean acidification or deoxygenation.

13  
14 In 2016, the Biogeochemical-Argo (BGC-Argo) program was launched with the goal  
15 to operate a global array of 1000 BGC-Argo floats equipped with oxygen (O<sub>2</sub>), chlorophyll *a*  
16 (Chl*a*) and nitrate (NO<sub>3</sub>) concentrations, particulate backscattering (b<sub>bp</sub>), pH and downwelling  
17 irradiance sensors (Biogeochemical-Argo Planning Group, 2016; Claustre et al., 2020).  
18 Although the planned number of 1000 floats has not been reached yet, the BGC-Argo  
19 program has already provided a large number of quality-controlled vertical profiles of O<sub>2</sub>,  
20 Chl*a*, NO<sub>3</sub>, b<sub>bp</sub>, and pH (Fig. 1). With respect to O<sub>2</sub>, Chl*a*, NO<sub>3</sub>, and b<sub>bp</sub>; the North Atlantic  
21 and the Southern Ocean are reasonably well sampled whereas pH is so far essentially sampled  
22 in the Southern Ocean. At regional scale, the Mediterranean Sea is also fairly well sampled by  
23 BGC-Argo floats (Salon et al., 2019; Terzić et al., 2019). However, there are still, large  
24 under-sampled areas, like the subtropical gyres or the sub-polar North Pacific. Nevertheless,  
25 the number of quality-controlled observations collected by the BGC-Argo fleet is already  
26 greater than any other data set (Claustre et al., 2020). The BGC-Argo data have also an  
27 unprecedented temporal and vertical resolution of key variables acquired simultaneously as  
28 well as a satisfactory level of accuracy and stability over time (Johnson et al., 2017; Mignot et  
29 al., 2019). Thanks to machine learning based methods (Bittig et al., 2018; Sauzède et al.,  
30 2017), floats equipped with O<sub>2</sub> sensors can be additionally used to derive, vertical profiles of  
31 NO<sub>3</sub>, phosphate (PO<sub>4</sub>), silicate (Si), alkalinity (Alk), dissolved inorganic carbon (DIC), pH  
32 and pCO<sub>2</sub>. All these specificities overcome the limitations of previous data sets from now and  
33 open new perspectives for the validation of BGC models (Gutknecht et al., 2019; Salon et al.,  
34 2019; Terzić et al., 2019).



1

2           We aim to demonstrate the use of the BGC-Argo global array for the validation of  
3 BGC models at the global scale. In regional seas or enclosed basins, where a limited number  
4 of floats have been so far deployed, point-by-point model-observation comparison is possible  
5 (Gutknecht et al., 2019; Salon et al., 2019). However, at the global scale, the BGC-Argo  
6 dataset provides a massive and ever-growing amount of data, and it can be difficult to  
7 manipulate this large data set, especially when it comes to evaluate a 3-D time-varying model  
8 simulation for about ten variables. In such cases, it is useful to define observationally-based  
9 metrics that are able to quantify the skill of a model to represent key oceanic processes  
10 (Russell et al., 2018). These metrics are quantities that summarize a particular process into a  
11 single number [e.g., the amplitude or the depth of an Oxygen Minimum Zone (OMZ)]. In this  
12 study, we present 18 metrics of ocean health and biogeochemical functioning for the  
13 assessment of a BGC model simulation. The metrics are either a depth-averaged quantity (e.g.,  
14 nutrients concentration,  $Chl a$ , ...) or correspond to the depth of a particular feature (e.g.,  
15 nitracline). These metrics are associated with the air-sea  $CO_2$  flux, the biological carbon  
16 pump, oceanic pH, oxygen levels and Oxygen Minimum Zones (OMZs).

17

18           The paper is organised as follow: section 2 presents the data sets used in the study. In  
19 section 3, we define the metrics necessary to compare the model to floats' observations. In  
20 section 4, we show examples of diagnostic plots for displaying the metrics. In section 5, we  
21 discuss metrics relative to optical properties in the water column. Finally, section 6  
22 summarizes and concludes the study.

23

## 24           **2. Data**

25

### 26                   **a. BGC-Argo floats observations**

27

28           The float data were downloaded from the Argo Coriolis Global Data Assembly Centre  
29 in France (<ftp://ftp.ifremer.fr/argo>). The CTD and trajectory data were quality controlled  
30 using the standard Argo protocol (Wong et al., 2015). The raw BGC signals were transformed  
31 to biogeochemical variables and quality-controlled according to international BGC-Argo  
32 protocols (Johnson et al., 2018b, 2018a; Schmechtig et al., 2015, 2018; Thierry et al., 2018;  
33 Thierry and Bittig, 2018).



1

2           In the Argo data-system, the data are available in three data modes, “Real-Time”,  
3           ”Adjusted” and ”Delayed” (Bittig et al., 2019). In the “Real-time” mode, the raw data are  
4           converted into state variable and an automatic quality-control has been applied to “flag” gross  
5           outliers. In the “Adjusted” mode, the “Real-time” data receive a calibration adjustment in an  
6           automated manner. In the “Delayed” mode, the “Adjusted” data are adjusted and validated by  
7           a scientific expert. While the “Real-Time” and “Adjusted” data are considered acceptable for  
8           operational application (data assimilation), the “Delayed” mode” is designed for scientific  
9           exploitation and represent the highest quality of data with the ultimate goal, when time-series  
10          with sufficient duration will have been acquired, to possibly extract climate-related trend.  
11          However, for some parameters, only a limited fraction of data is accessible in “Delayed-  
12          Mode”. Consequently, for each parameter, we selected the highest quality of data that did not  
13          compromise too much the number of observations available (see Table 1). We removed data  
14          with missing location or time information and flagged as “Bad data” (flag =4). Depending on  
15          the parameter and the associated data mode, we also excluded data flagged as “potentially bad  
16          data” (flag=3) (see Table 1).

17

18           Particulate Organic Carbon (POC) concentrations were derived from  $b_{bp}$  observations.  
19          First, three consecutive low-pass filters were applied on the vertical profiles of  $b_{bp}$  to remove  
20          spikes (Briggs et al., 2011): a 2-points running median followed by a 5-points running  
21          minimum and 5-points running maximum. Then, the filtered  $b_{bp}$  profiles were converted into  
22          POC using the relationship proposed by Cetinic et al. (2012), i.e.  $POC=35422 * b_{bp}-14.4$ .  
23          Negative values resulting from this transformation were set to 0.

24

25           Finally, we complemented the existing BGC-Argo dataset with pseudo-observations  
26          of  $NO_3$ ,  $PO_4$ , Si, and DIC concentrations as well pH and  $pCO_2$  using the CANYON-B neural  
27          network (Bittig et al., 2018). CANYON-B estimates vertical profiles of nutrients as well as  
28          the carbonate system variables from concomitant measurements of floats pressure,  
29          temperature, salinity and  $O_2$  qualified in “Delayed “mode together with the associated  
30          geolocation and date of sampling.

31

32

33           **b. CMEMS global BGC Model**



1

2           The global model simulation used in this study (see Appendix A.1) originates from the  
3 Global Ocean hydrodynamic-biogeochemical model, implemented and operated by the Global  
4 Monitoring and Forecasting Center of the EU, the Copernicus Marine Environment  
5 Monitoring Service (CMEMS). It is based on the coupled NEMO–PISCES model and it is  
6 constrained by the assimilation of satellite Chl $a$  concentrations. The BGC model is forced  
7 offline by daily fields of ocean, sea ice and atmosphere. The ocean and sea ice forcing come  
8 from Mercator Ocean global high-resolution ocean model (Lellouche et al., 2018) that  
9 assimilates along-track altimeter data, satellite Sea Surface Temperature and Sea-Ice  
10 Concentration, and *in situ* temperature and salinity vertical profiles. The BGC model has a  
11 1/4° horizontal resolution, 50 vertical levels (with 22 levels in the upper 100 m, the vertical  
12 resolution is 1m near the surface and decreases to 450m resolution near the bottom). It  
13 produces daily outputs of Chl $a$ , NO $_3$ , PO $_4$ , Si, O $_2$ , pH, DIC and Alk, and weekly outputs of  
14 POC (resampled offline from weekly to daily frequency through linear interpolation) from  
15 2009 to 2017. The POC model used in this study corresponds to the sum two size classes of  
16 particulate organic matter modelled by PISCES (Aumont et al., 2015). Partial pressures of  
17 CO $_2$  values are calculated offline from the modelled DIC, Alk, temperature and salinity data  
18 using the seacarb program for R (<https://CRAN.R-project.org/package=seacarb>). The Black  
19 Sea was not taken into account in the present analysis because the model solutions are of very  
20 poor qualities. Finally, the daily model outputs were collocated in time and the closest to the  
21 BGC-Argo floats positions, and they were interpolated to the sampling depth of the float  
22 observations. The characteristics of the model are further detailed in the appendix.

23

### 24           **3. Metrics**

25

26           In this section, we present 18 key metrics of ocean health and biogeochemical  
27 functioning. The metrics are associated with the air-sea CO $_2$  flux, the biological carbon pump,  
28 oceanic pH, oxygen levels and Oxygen minimum zones (OMZs). The metrics are described  
29 below and summarized in Table 2.

30

#### 31           **a. Air-sea CO $_2$ flux**

32



1           The air-sea CO<sub>2</sub> flux is generally calculated following a bulk formulation  
2 (Wanninkhof, 2014),  $F_{CO_2} = k\alpha(pCO_{2atm} - spCO_2)$ , where  $F_{CO_2}$  is the air-sea CO<sub>2</sub> flux,  $\alpha$  is the  
3 CO<sub>2</sub> solubility in seawater,  $k$  is a gas transfer coefficient that depends on wind speed,  $spCO_2$   
4 is the partial pressure of CO<sub>2</sub> at the ocean's surface, and  $pCO_{2atm}$  is the partial pressure of  
5 CO<sub>2</sub> in the atmosphere. Among the uncertainties affecting the different components of the  
6 model CO<sub>2</sub> flux, BGC-Argo data can contribute to estimate that on  $spCO_2$ . Thus, the  
7 validation of  $pCO_2$  plays a critical role to assess the skill of a BGC model in representing  
8 correctly the air-sea CO<sub>2</sub> flux.

9

10           Here,  $spCO_2$  is defined as the average of  $pCO_2$  profile between the surface and the  
11 mixed layer depth (MLD). Following De Boyer et al. (2004), the MLD is computed as the  
12 depth at which the change in potential density from its value at 10 m exceeded  $0.03 \text{ kg m}^{-3}$ .

13

#### 14           **b. Oceanic pH**

15

16           Ocean acidification is the decrease in oceanic pH due to the absorption of  
17 anthropogenic CO<sub>2</sub>. The acidification of the ocean is expected to impact primarily the surface  
18 oceanic waters as well as the 200-400 m layer (Kwiatkowski et al., 2020). Assessing how  
19 models correctly represent oceanic pH at the surface is therefore critical if we aim to derive  
20 accurate climate projections on acidification. The surface ocean pH ( $spH$ ) is defined as the  
21 average of pH profile between the surface and the base of the mixed layer and the pH in the  
22 200-400 m layer ( $pH_{200-400}$ ) as the average of pH profile in this layer.

23

#### 24           **c. Biological carbon pump**

25

26           The biological carbon pump is the transformation of nutrients and dissolved inorganic  
27 carbon into organic carbon in the upper part of the ocean through phytoplankton  
28 photosynthesis and its subsequent transfer of this organic material into the deep ocean.

29           A useful way to investigate the biological carbon pump is to look at the depth-  
30 averaged concentrations in nutrients ( $NO_3$ ,  $PO_4$ , and Si), DIC,  $Chl a$  and POC computed from  
31 the surface down to the MLD, hereinafter denoted  $sNO_3$ ,  $sPO_4$ ,  $sSi$ ,  $sDIC$ ,  $sChl$  and  $sPOC$ . To  
32 assess the quantity of POC that is exported to the deep ocean, we compute the mesopelagic



1 POC concentration ( $\text{POC}_{\text{meso}}$ ), which correspond to the depth-averaged POC concentrations  
2 between the base of the mixed layer down to 1000 m (Dall’Olmo and Mork, 2014).

3  
4 At the base of the euphotic layer of stratified systems, a *Chl a* maximum (hereinafter  
5 denoted Deep Chlorophyll Maximum, DCM) develops that generally escapes detection by  
6 remote sensing (Barbieux et al., 2019; Cullen, 2015; Letelier et al., 2004; Mignot et al., 2014,  
7 2011). It has been suggested that the DCM plays an important role in the synthesis of organic  
8 carbon by phytoplankton (Macías et al., 2014). The DCM is therefore an important feature to  
9 be assessed in BGC models with respect to the production of organic carbon and more  
10 generally to the biological carbon pump. The depth and magnitude of DCM ( $H_{\text{dcm}}$  and  $\text{Chl}_{\text{dcm}}$ )  
11 are helpful metrics for the assessment of DCM dynamics. The depth of the DCM is calculated  
12 as the depth where the maximum of *Chl a* occurs in the profile with the criterion that  $H_{\text{dcm}}$   
13 should be deeper than  $H$ . The magnitude of the DCM is computed at the value at  $H_{\text{dcm}}$ .  
14 Finally, the depth of nitracline ( $H_{\text{nit}}$ ) is also evaluated as it is an important driver for  $H_{\text{dcm}}$  and  
15  $\text{Chl}_{\text{dcm}}$  (Barbieux et al., 2019; Herbland and Voituriez, 1979). Following Richardson and  
16 Bentsen (2019),  $H_{\text{nit}}$  was computed at the depth at which  $\text{NO}_3 = 1 \mu\text{mol kg}^{-1}$ .

17

#### 18 **d. Oxygen levels and oxygen minimum zones**

19

20 Oxygens levels in the global and coastal waters have declined over the whole water  
21 column over the past decades (Schmidtko et al., 2017) and OMZs are expanding (Stramma et  
22 al., 2008). Assessing how models correctly represent ocean oxygen levels as well as the  
23 OMZs is therefore critical. We evaluate oxygen levels in 3 layers, at the surface, at 300 m and  
24 at 1000 m. The surface  $\text{O}_2$  ( $s\text{O}_2$ ), important for the air-sea  $\text{O}_2$  flux, is defined as the average  
25 of  $\text{O}_2$  profile in the mixed layer. The oxygen at 300 m ( $\text{O}_{2\ 300}$ ), a depth where large areas of  
26 the global ocean have very low  $\text{O}_2$  (Breitburg et al., 2018), is defined as the average of  $\text{O}_2$   
27 profile between 250 and 300 m. The deep oxygen content, ( $\text{O}_{2\ 1000}$ ), is defined as the average  
28 of  $\text{O}_2$  profile between 950 and 1000 m. Finally, to characterize the OMZs, we evaluate the  
29 depth ( $H_{\text{O}_2\text{min}}$ ) and concentration ( $\text{O}_{2\text{min}}$ ) of  $\text{O}_2$  minimums.  $\text{O}_2$  level lower than  $80 \mu\text{mol kg}^{-1}$   
30 are used to characterize OMZs (Schmidtko et al., 2017).

31

#### 32 **4. Diagnostic plots to display the BGC-Argo based metrics**



1

2       Based upon the existing literature (e.g., Aumont et al., 2015; Cossarini et al., 2019; Doney  
3 et al., 2009; Dutkiewicz et al., 2015; Gutknecht et al., 2019; Salon et al., 2019; Séférian et al.,  
4 2013; Terzić et al., 2019), we propose 4 graphical representations that can be used to display  
5 the novel validation metrics and to assess the skill of a model in reproducing a particular  
6 process or variable: Taylor diagrams, scatterplots, spatial maps, and time series.

7

### 8           **a. Taylor diagram**

9

10       Taylor diagrams are useful to display simultaneously information on model-data skill  
11 for a suite of metrics (Taylor, 2001). These diagrams combine the Pearson correlation  
12 coefficient ( $r$ ), root-mean-square difference (RMSD) and the model standard deviation (SD).  
13 In order to represent all metrics with different units into a single diagram, we use a  
14 normalized Taylor diagram (RMSD and the model SD are divided by the SD of the  
15 observations). In the diagram, the Pearson correlation coefficient between the model and the  
16 observations is related to the azimuthal angle. The normalized SDs are proportional to the  
17 radial distances from the origin. The observational reference is indicated along the x-axis and  
18 corresponds to the normalized SD and  $r=1$ . Finally, the normalized RMSD is proportional to  
19 the distance from the observational difference.

20

### 21           **b. Scatter/Density plots**

22

23       In validation exercises, scatter plots are useful to identify relationships between the  
24 predicted and observed values. It is common to add a least squares regression line to quantify  
25 the strength of the linear relationship between the observed and predicted values. Scatter plots  
26 are also helpful to show other patterns in data, such as non-linear relationships, clusters of  
27 points and outliers. In those cases, when a large amount of data points has to be plotted (like  
28 in our study), the points overlap to a degree where it can be difficult to distinguish the  
29 relationship between the variables. To overcome this, scatter plots are displayed as density  
30 plots, where each axis is divided in a number of bins while the colour within each bin  
31 indicates the number of points.

32

### 33           **c. Spatial maps**



1  
2           Spatial maps draw attention to the spatial distribution of a given metric. The maps are  
3 handy to determine if the model is skilled in reproducing global patterns, spatial gradients,  
4 and basins inter-difference. It is also helpful to display the BIAS and RMSD between  
5 predicted and observed values on a spatial map to quickly determine regions where the model  
6 uncertainty is the highest. Depending on the context, the comparison between the model and  
7 the observation can be performed either on a climatological level, or for a specific period  
8 (year, month, etc ..). In our case, the scarcity of observations imposes us to display all data  
9 (from 2009 to 2017; the period of analysis of the model simulation) in a climatological way if  
10 we want to highlight large scale patterns. To do so, the metrics from 2009 to 2017 are  
11 averaged in  $4^{\circ} \times 4^{\circ}$  bins, bins with less than 4 points being not included. We also computed the  
12 BIAS and RMSD within each bin.

13

#### 14           **d. Seasonal time-series**

15

16           Taylor diagrams, scatter plots and spatial maps are powerful diagnostics plots to  
17 evaluate the global skills of a model but understanding the causes of difference remains  
18 somewhat limited with these diagrams. Rather, the comparative analysis of seasonal time-  
19 series of multiple metrics and their inter-relationships is a powerful tool to highlight and to  
20 understand BGC processes. This is especially true for the biological carbon pump that has a  
21 strong seasonal variability due to the seasonal variation in sunlight, surface heating and  
22 surface wind (Williams and Follows, 2011). As a matter of fact, the analysis of seasonal  
23 dynamics in nutrients as well as in phyto- and zoo- plankton has a rich history for the  
24 development of BGC model (Evans and Parslow, 1985; Riley, 1946).

25

### 26           **5. Results: Application to CMEMS global model**

27

28           Examples of the diagnostic plots described in section 4 in combination with the metrics  
29 defined in Section 3 are shown. The objective of this section is to illustrate the opportunities  
30 offered by the BGC-Argo-based metrics for evaluating global BGC model solutions, rather  
31 than to provide a full evaluation of the CMEMS global model. Consequently, for each  
32 diagnostic plot, we only present one detailed example. The density plots and spatial maps for  
33 all metrics are displayed in the Appendix section (Fig. A1-A36).



1

2

### a. Taylor diagram

3

4 The CMEMS global model skill is summarized in the normalized Taylor diagram  
5 (Fig. 2). The oxygen levels metrics ( $sO_2$ ,  $O_{2\ 300}$ ,  $O_{2\ 1000}$ ),  $pH_{200-400}$ , the average nutrients and  
6 DIC concentrations in the mixed layer are particularly well represented in the model. The  
7 correlation coefficients are greater than 0.95, the predicted SDs are close the observed SDs  
8 and the normalized RMSDs are lower than 0.4. The OMZs as well as the depths of DCM and  
9 nitracline are reasonably well represented in the model, with  $r > 0.9$  (OMZs) and  $r > 0.8$  (for  
10  $H_{nit}$  and  $H_{dcm}$ ) and normalized RMSDs  $< 0.6$ . The variability in the predicted  $O_{2min}$  is however  
11 larger than the observed ones. Finally, the POC concentrations, the Chl $a$  in the mixed layer  
12 and at the DCM as well as  $spCO_2$  and  $spH$  are the worst predicted metrics. The normalised  
13 RMSD is greater than 0.7-0.8,  $r$  is between 0.4 and 0.6, and the amplitude of model variations  
14 is lower than the BGC-Argo observations.

15

16 The representation of all metrics into a single Taylor diagram allows to rapidly  
17 evaluate the strengths and the weaknesses of a model simulation. For instance, the CMEMS  
18 global model is skilled in reproducing oxygen levels and the cycling of nutrients and DIC in  
19 the mixed layer, but the representation of Chl $a$  and POC needs to be improved.

20

### b. Scatter/Density plots

21

22 The density plots for all metrics are displayed in the Appendix section (Fig. A1-A18).  
23 Here, we detail only the density plot for  $O_{2min}$  to illustrate the potential of such representations.

24

25 Figure 3 shows the comparison between the observed and predicted  $O_{2min}$  values. The  
26 regression line, the slope, and the intercept as well the coefficient of determination ( $R^2$ ) are  
27 indicated. Overall, the model and the float  $O_{2min}$  are in good agreement with a slope close to 1  
28 and  $R^2$  close to 0.8. There is however a positive offset of  $\sim 11\ \mu\text{mol kg}^{-1}$  across all  $O_{2min}$  values  
29 suggesting that the modelled OMZs are on average too much oxygenated by a constant value.  
30 It is worth noting that the scatter around the regression line is larger for  $O_{2min} > 50\ \mu\text{mol kg}^{-1}$ ,  
31 which corresponds to the Atlantic OMZ around the Cap Verde Archipelago (Fig. A35). This  
32 suggests that the uncertainty in this OMZ is particularly high, as confirmed in Fig. A35.  
33



1

2

### c. Spatial maps

3

4

The spatial maps for all metrics are displayed in the Appendix section (Fig. A19-A36), while we detail hereafter the spatial distribution of sChl.

6

7

Figure 4 shows the spatial distribution of sChl estimated from the BGC-Argo floats (Fig. 4a), the model (Fig. 4b), the BIAS (Fig. 4c) and the RMSD (Fig. 4d). As already noticed in Fig. 1, the density of sChl observations is satisfactory for high latitude regions (latitudes > 50° N and S) whereas it is poor in subtropical gyres and the Equatorial band. Nevertheless, large scale patterns in sChl are still distinguishable in Fig. 1a, especially the juxtaposition of the high-latitudes-high- sChl regions with the low-latitudes-low- sChl regions. The model (Fig. 4b) exhibits large-scale, coherent patterns. However, the model tends to be lower than the BGC-Argo observations in the high-latitudes region and higher in the subtropical gyres (Fig. 4c). The RMS difference between the predicted and the observed values seems to be quite uniform, suggesting the uncertainty in model sChl is fairly constant in all oceanic basins.

18

19

### d. Seasonal time-series

20

21

An example of a BGC-Argo float seasonal time-series compared to a simulation of the same time-series along the float trajectory is presented in Fig. 5 for a case study in the North Atlantic during the “spring bloom” .

24

25

26

27

28

29

30

31

32

33

Figure 5 compares the seasonal time series of MLD, sChl, sNO<sub>3</sub>, sSi and sPO<sub>4</sub> derived from the BGC-Argo floats observations (blue) and from the model simulation (yellow). The seasonal cycle of MLD, sChl and nutrients is typical of the North Atlantic bloom dynamics (Dale et al., 1999; Mignot et al., 2018). In spring, phytoplankton concentration, as measured by sChl increases dramatically and it is accompanied by a consumption of inorganic nutrients in the mixed layer. The increase in sChl stops when one or several nutrients become exhausted and the nutrients-Chl<sub>a</sub> system remains in an equilibrium phase. In fall, as the mixed layer starts deepening, deep nutrients and inorganic carbon are entrained in the surface layer driving an increase in surface concentrations. However, the



1 decrease in sea surface light and the increase in upper ocean mixing drive phytoplankton cells  
2 away from the well-lit surface inducing a decrease in phytoplankton abundance and thus sChl.

3  
4 The seasonal cycle of sChl and nutrients is well approximated by the model with the  
5 timings of minima, maxima and the onset of the bloom being correctly represented. The  
6 winter- sChl -minimum and winter-nutrients-maxima are also properly estimated by the  
7 model. However, the summer- sChl -maximum is underestimated and the summer- sNO<sub>3</sub> -  
8 minimum and summer- sPO<sub>4</sub> -minimum are overestimated while the summer- sSi -minimum  
9 is correctly represented. This explain the negative BIASs observed in the spatial map of sChl  
10 in the North Atlantic (Fig. 4) and the positive BIAS in the spatial map of sNO<sub>3</sub> and sPO<sub>4</sub> in  
11 the North Atlantic (Figs. A23 and A24).

12  
13 The conjoint analysis of the seasonal times-series of Chl*a* and nutrients strongly  
14 suggest that modelled rates of primary production are too weak in summer so that sNO<sub>3</sub> and  
15 sPO<sub>4</sub> are not consumed fast enough by phytoplankton. The summer sSi being correctly  
16 estimated, we can also hypothesized that the main phytoplankton class in the model  
17 consuming Si, i.e; the diatoms (Aumont et al., 2015), are well represented whereas the other  
18 phytoplankton class in the model , i.e., nanophytoplankton, are misrepresented during  
19 summer. The reasons for this could be that nanophytoplankton growth rates are too weak or  
20 that grazing on nanophytoplankton is too strong.

21  
22 The underestimation in the rates of primary production has a direct impact on the  
23 oceanic carbon cycle in the North Atlantic (Fig. 6). The summer sDIC are higher in the model  
24 compared to the BGC-Argo estimates. Similarly, the summer sPOC concentrations are too  
25 low, suggesting that the uptake of atmospheric CO<sub>2</sub> and the transformation of dissolved  
26 inorganic carbon into organic carbon are too weak in the model during summer. However,  
27 this seems to have a limited effect on the export of POC to the deep ocean as the modelled  
28 POC concentrations in the mesopelagic layer are consistent with the BGC-Argo observations  
29 during summer.

30

## 31 **6. Perspectives: metrics relative to ocean optical properties**

32



1 BGC-Argo floats equipped with sensors measuring the downward planar irradiance are  
2 essential observations to evaluate the performance of recently-developed BGC models that  
3 resolve the spectral and directional properties of the underwater light field. For several years,  
4 the number of BGC models coupled with a multispectral light module has been steadily  
5 increasing (Baird et al., 2016; Dutkiewicz et al., 2015; Gregg and Rousseaux, 2016; Lazzari et  
6 al., 2020; Skákala et al., 2020). Such models require dedicated observations and metrics to  
7 evaluate their skill in representing the ocean's optical properties of the ocean. Diffuse  
8 attenuation coefficient for downwelling irradiance ( $K_d$ ) is one of the most common properties  
9 to characterise the optical state of the ocean (Sosik, 2008). Values of  $K_d$  can be derived at  
10 three different wavelengths (380, 412, 490 nm) from the BGC-Argo floats observations. This  
11 metric also provides information about the constituents of seawater (Organelli 2017)  
12 (phytoplankton for  $K_d$  at 490 nm and coloured dissolved organic carbon for  $K_d$  at 380 nm and  
13 412 nm) and is complementary to  $Chl_a$  measurements for the assessment of the modelled  
14 phytoplankton dynamics.

15

16 As an example of the potentiality of such comparison, spatial distribution of  $K_d$  at 490  
17 nm in the first optical depth estimated from the BGC-Argo floats and from a model of the  
18 Mediterranean Sea equipped with a multispectral light module (Lazzari et al., 2020)  
19 (Appendix A.2) are shown in Fig. 7. The BGC-Argo estimated  $K_d$  at 490 nm exhibits a basin-  
20 scale pattern, with high values in the North-Western Mediterranean Sea and lower values in  
21 the Eastern Mediterranean Sea, consistent with the spatial distribution of surface  $Chl_a$  in the  
22 Mediterranean Sea (Bosc et al., 2004). The model is able to reproduce the large-scale pattern  
23 of  $K_d$  at 490 nm, but it tends to underestimate  $K_d$  at 490 nm in the North-Western  
24 Mediterranean Sea; area where the RMSD is also the highest. The annual cycle of  
25 phytoplankton being largely influenced by a spring bloom in this region (Bosc et al., 2004;  
26 D'Ortenzio et al., 2014), we can speculate that the underestimation of  $K_d$  at 490 nm highlights  
27 a possible misrepresentation of the spring bloom in the model that yields to lower  
28 phytoplankton and  $Chl_a$  concentrations.

29

## 30 **7. Conclusion**

31

32 Biogeochemical ocean models are powerful tools to monitor changes in marine  
33 ecosystems and ecosystem health due to human activities, make climate projections and help



1 developing better strategies for mitigation. However, these models are subject to flaws and  
2 require rigorous validation processes to test their predictive skills. The model's evaluations  
3 have long been damped by the lack of *in situ* observations, which has certainly slowed the  
4 development and the improvement of BGC models. The amount of observations collected by  
5 the BGC-Argo program is now greater than any other *in situ* data set (Claustre et al., 2020)  
6 and thus offers new opportunities for the validation of BGC models.

7  
8 In this study, we use the global data set of BGC-Argo observations to validate a state-of-  
9 the-art BGC model simulation. Our aim was to demonstrate the invaluable opportunities  
10 offered by the BGC-Argo observations for evaluating global BGC model solutions. To ease  
11 the comparison between model and observations at global scale, we proposed 18 key metrics  
12 of ocean health and biogeochemical functioning. These metrics are either a depth-averaged  
13 quantity or correspond to the depth of a particular feature. We did not propose BGC-Argo-  
14 based phenology metrics (Gittings et al., 2019), because the numbers of observation per  
15 month and per bin is still presently too low, to derive such robust metrics. We suggested 4  
16 diagnostic plots, which we believe are particularly suitable for displaying the metrics in  
17 support of identification of model-data difference and subsequent analysis of model  
18 representativity. We also discuss the promising avenue of BGC-Argo-based metrics relative  
19 to optical properties in the ocean for the validation of the new generation of BGC model  
20 equipped with a multispectral light module.

21  
22 We assumed that the differences between the observed and predicted BGC values were  
23 only attributable to the BGC model, PISCES. However, BGC models are coupled to ocean  
24 general circulation systems and the quality of the BGC predictions strongly depends on the  
25 accuracy of the physical properties that control the BGC state variables. In our case, the  
26 dynamical component has been extensively validated (Lellouche et al., 2018, 2013), and  
27 correctly represented variables that are constrained by observations (e. g., temperature and  
28 salinity). However, unconstrained variables in the physical system (e.g., vertical velocities)  
29 can generate unrealistic biases in various biogeochemical variables, especially in the  
30 Equatorial Belt area (Fennel et al., 2019; Park et al., 2018).

31  
32 In addition, BGC-Argo floats are not flawless (Roesler et al., 2017), and in some cases,  
33 the discrepancies observed between the floats and model data do not result from the model  
34 estimations alone. This is particularly true for the BGC-Argo estimates of Chl $a$  in the mixed



1 layer that can be significantly biased due to non-photochemical chlorophyll fluorescence  
2 quenching (Xing et al., 2012) or regional variations in fluorescence of Chla vs Chla  
3 relationship (Roesler et al., 2017).

4

5 We have restricted the number of diagnostic plots as well the statistical indices to the ones  
6 that are most commonly used in the modelling community. More complex statistical  
7 indicators (Stow et al., 2009) can be computed with the proposed metrics, depending on the  
8 context and the skill level necessary. Likewise, similar or more elaborate diagrams can also be  
9 used, such as Target diagram (Salon et al., 2019), zonal mean diagrams (Doney et al., 2009),  
10 or interannual time series (Doney et al., 2009).

11

12 The comparison between BGC-Argo data and model simulations is not only beneficial  
13 for the modelling community but also for the BGC-Argo community. Observation System  
14 Simulation Experiments (OSSEs) are generally used to inform, *a priori*, observing network  
15 design (Ford, 2020). Here, we showed that model-observations comparison is, also  
16 informative, *a posteriori*, with respect to the network design, as it highlights sensitive areas  
17 where BGC-Argo observations are critical and where sustained BGC-Argo observations are  
18 required to better constrain the model. It corresponds to the regions where the model  
19 uncertainty (see RMSD spatial maps in Figs. A19-A36) is the highest, i.e., the Equatorial  
20 band with respect to the carbonate system variables, the Southern Ocean with respect to the  
21 nutrients and the DCM variables and the western boundary currents and OMZs with respect to  
22 oxygen.

23



1 **Tables**

2

3 **Table 1.** Data mode and QC flags of the BGC-Argo observations used in this study.

4

Parameter	Data mode	Date mode of associated pressure, temperature and salinity profiles	QC flags
Chla	Adjusted and Delayed	Real time, Adjusted and Delayed	<ul style="list-style-type: none"> <li>• Real time: All flags except 4</li> <li>• Adjusted or Delayed: All flags except 3 and 4</li> </ul>
O <sub>2</sub>	Delayed	Delayed	<ul style="list-style-type: none"> <li>• All flags except 3 and 4</li> </ul>
NO <sub>3</sub>	Adjusted and Delayed	Real time, Adjusted and Delayed	<ul style="list-style-type: none"> <li>• Real time: All flags except 4</li> <li>• Adjusted or Delayed: All flags except 3 and 4</li> </ul>
pH	Adjusted and Delayed	Real time, Adjusted and Delayed	<ul style="list-style-type: none"> <li>• Real time: All flags except 4</li> <li>• Adjusted or Delayed: All flags except 3 and 4</li> </ul>
b <sub>bp</sub>	Real time and Delayed	Real time, Adjusted and Delayed	<ul style="list-style-type: none"> <li>• Real time: All flags except 4</li> <li>• Adjusted or Delayed (P,T,S): All flags except 3 and 4</li> <li>• Adjusted or Delayed (b<sub>bp</sub>): All flags 4</li> </ul>

5



1

2 **Table 2.** BGC-Argo metrics used to assess the model simulation

3

Process	Metric	Definition	units
Air-sea CO <sub>2</sub> flux	spCO <sub>2</sub>	Depth-averaged pCO <sub>2</sub> in the mixed layer	µatm
Oceanic pH	spH	Depth-averaged pH in the mixed layer	total
	pH <sub>200-400</sub>	Depth-averaged pH in the 200-400 m layer	total
Biological carbon pump	sChl	Depth-averaged Chl <sub>a</sub> in the mixed layer	mg m <sup>-3</sup>
	sNO <sub>3</sub>	Depth-averaged NO <sub>3</sub> in the mixed layer	µmol kg <sup>-1</sup>
	sPO <sub>4</sub>	Depth-averaged PO <sub>4</sub> in the mixed layer	µmol kg <sup>-1</sup>
	sSi	Depth-averaged Si in the mixed layer	µmol kg <sup>-1</sup>
	sDIC	Depth-averaged DIC in the mixed layer	µmol kg <sup>-1</sup>
	sPOC	Depth-averaged POC in the mixed layer	mg m <sup>-3</sup>
	POC <sub>meso</sub>	Depth-averaged POC in the mesopelagic layer	mg m <sup>-3</sup>
	Chl <sub>DCM</sub>	Magnitude of DCM	mg m <sup>-3</sup>
	H <sub>DCM</sub>	Depth of DCM	m
H <sub>nit</sub>	Depth of nitracline	m	
Oxygen levels and OMZs	sO <sub>2</sub>	Depth-averaged O <sub>2</sub> in the mixed layer	µmol kg <sup>-1</sup>
	O <sub>2 300</sub>	O <sub>2</sub> at 300 m	µmol kg <sup>-1</sup>
	O <sub>2 1000</sub>	O <sub>2</sub> at 1000 m	µmol kg <sup>-1</sup>
	O <sub>2min</sub>	value of O <sub>2</sub> minimum	µmol kg <sup>-1</sup>
	H <sub>O2min</sub>	Depth of O <sub>2</sub> minimum	m

4

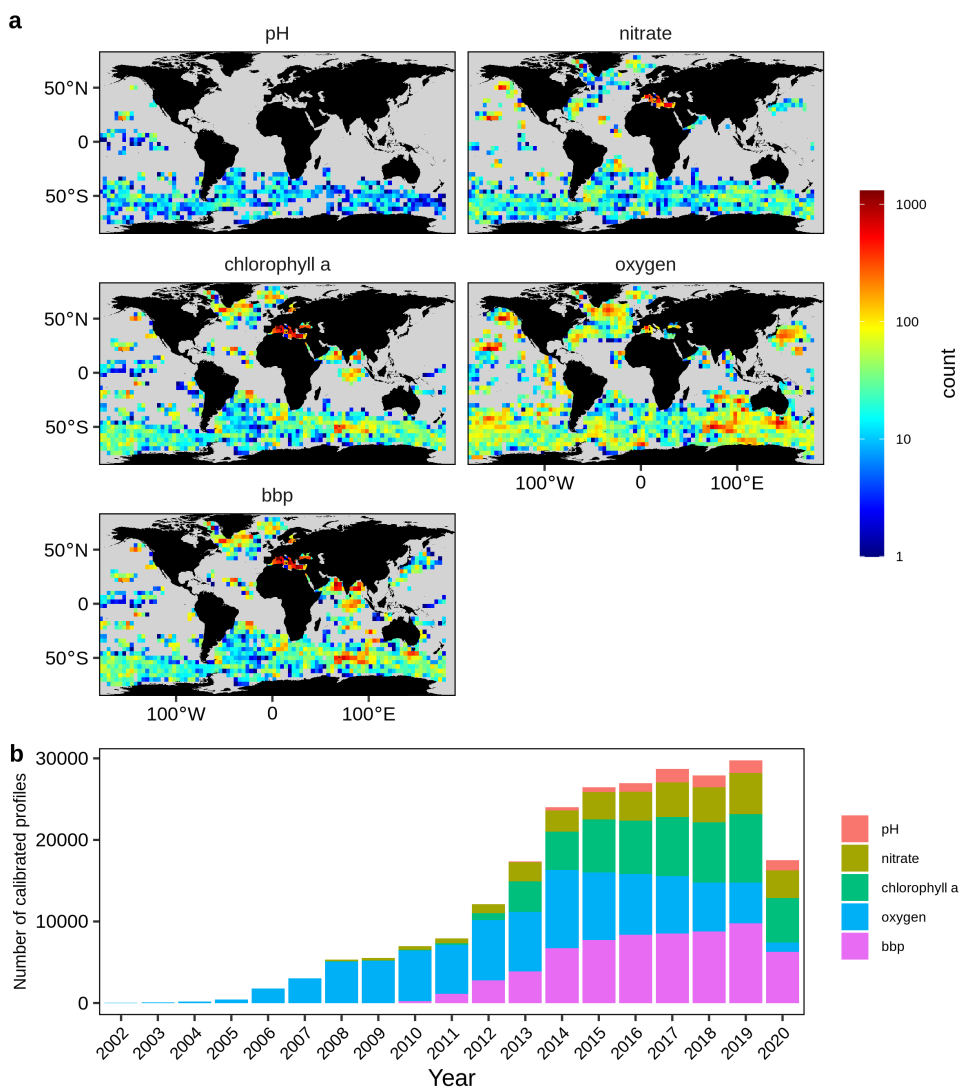
5



1

## 2 Figures

3

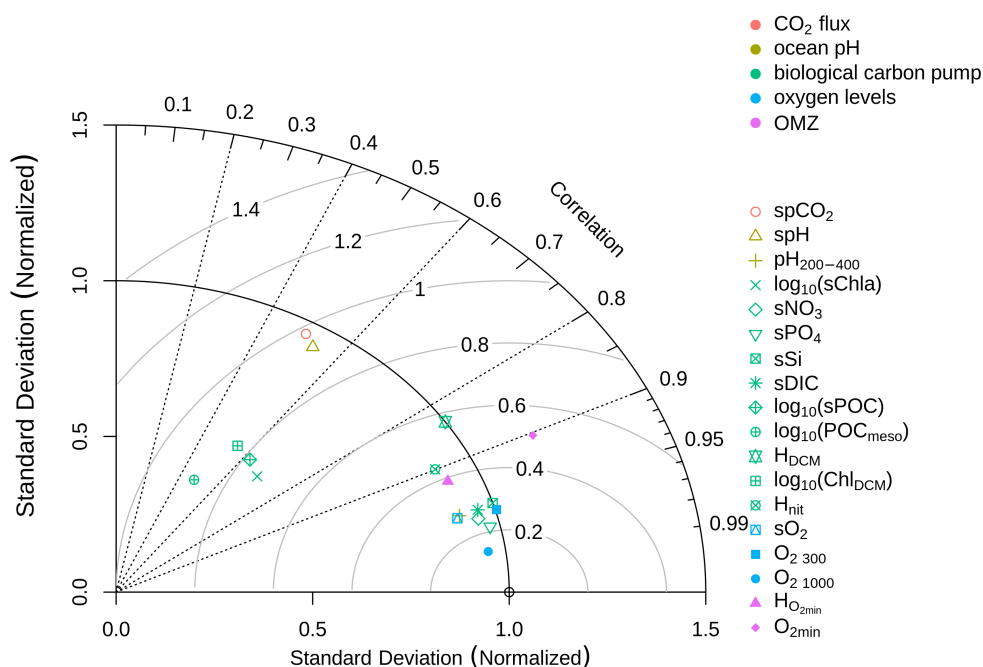


4

5

6 **Figure 1.** Spatial and temporal coverage of quality-controlled BGC-Argo pH, NO<sub>3</sub><sup>-</sup>, Chla, O<sub>2</sub>,  
7 and b<sub>bp</sub> profiles. **(a)** Number of quality-controlled profiles for the entire period per 4°x4° bin.

8 **(b)** Number of quality-controlled profiles per year.



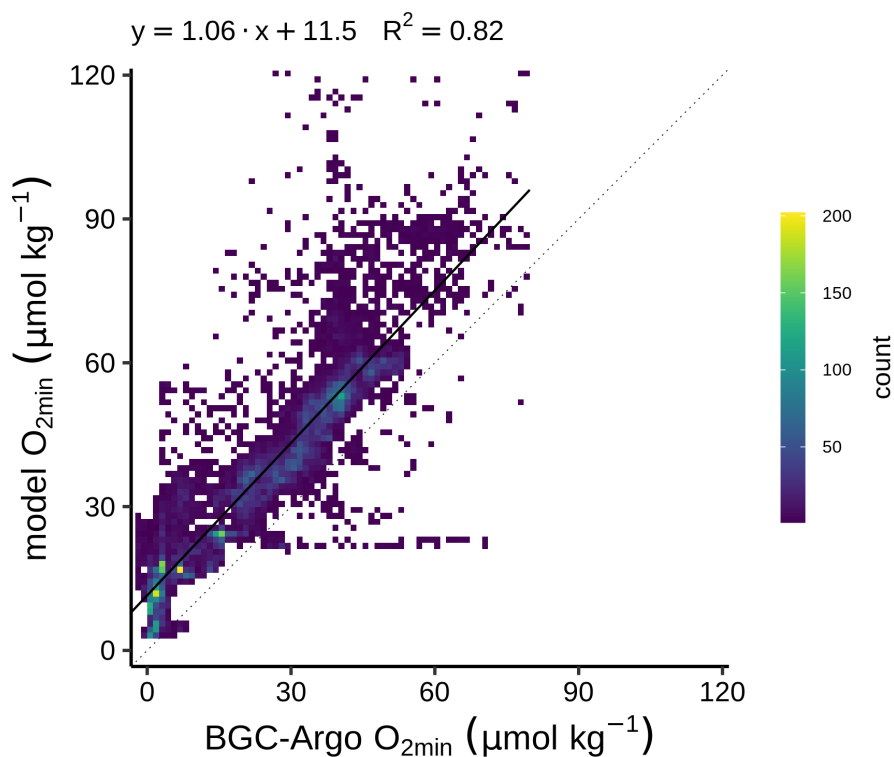
1

2

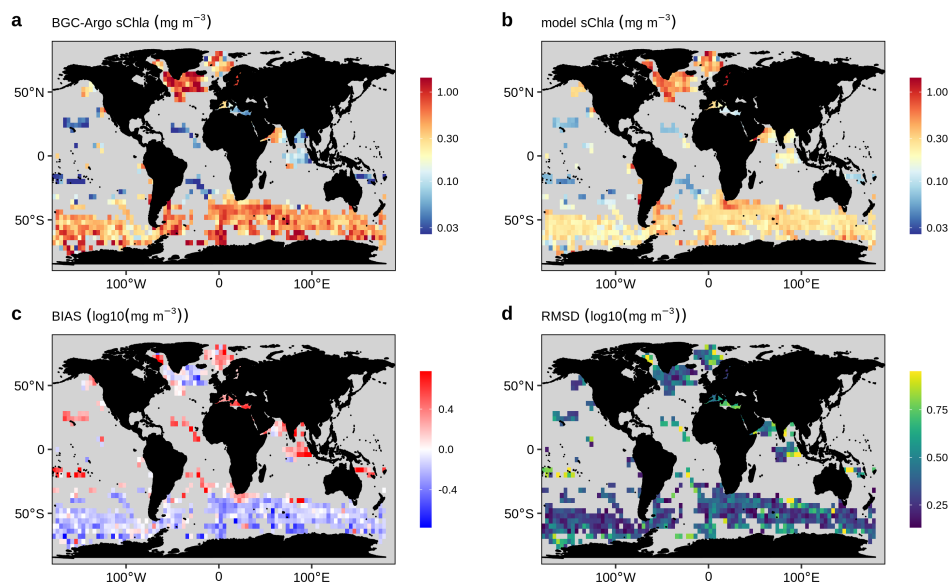
3 **Figure 2.** Comparison of BGC-Argo floats' observations and model values for all metrics  
 4 using Taylor diagram. The symbols correspond to the metrics and the colours represent the  
 5 BGC processes with which they are associated. Note that the metrics calculated from the float  
 6 pH and NO<sub>3</sub> used both the direct observations of the floats and as well as the estimations from  
 7 CANYON-B. The metrics related to Chl<sub>a</sub> and POC, namely sChl, Chl<sub>DCM</sub>, sPOC, POC<sub>meso</sub>  
 8 were log<sub>10</sub>-transformed because they cover several orders of magnitude and they are  
 9 lognormally distributed. Observed DCMs and nitracline deeper than 250 m are not included.

10

11

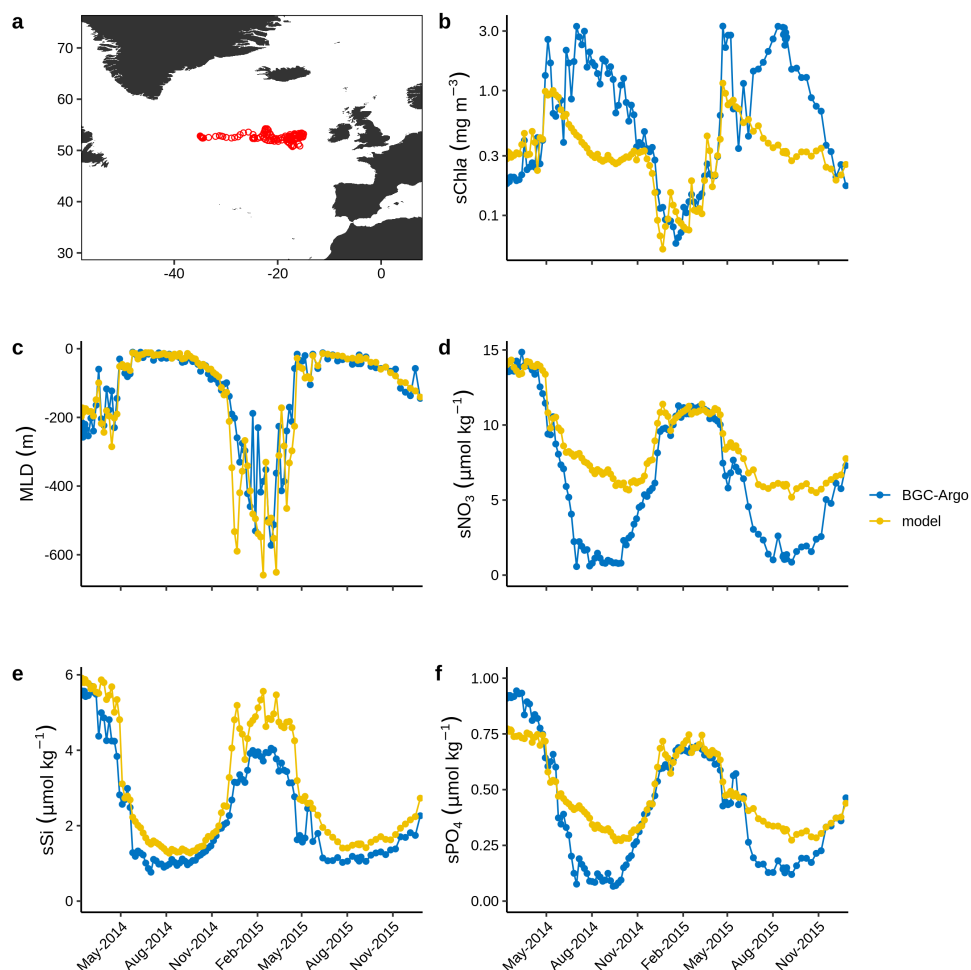


1  
2 **Figure 3.** Density plots of BGC-Argo floats' observations and model  $O_{2min}$ . Each axis is  
3 divided in 100 bins and the colour represents the number of points in each bin. The dashed  
4 line represents the 1:1 line. The plain line represents the linear regression line between the  
5 two data sets. The coefficients of the linear regression line (gain and offset) as well the  
6 coefficient of determination ( $R^2$ ) are indicated on the top of the plot.



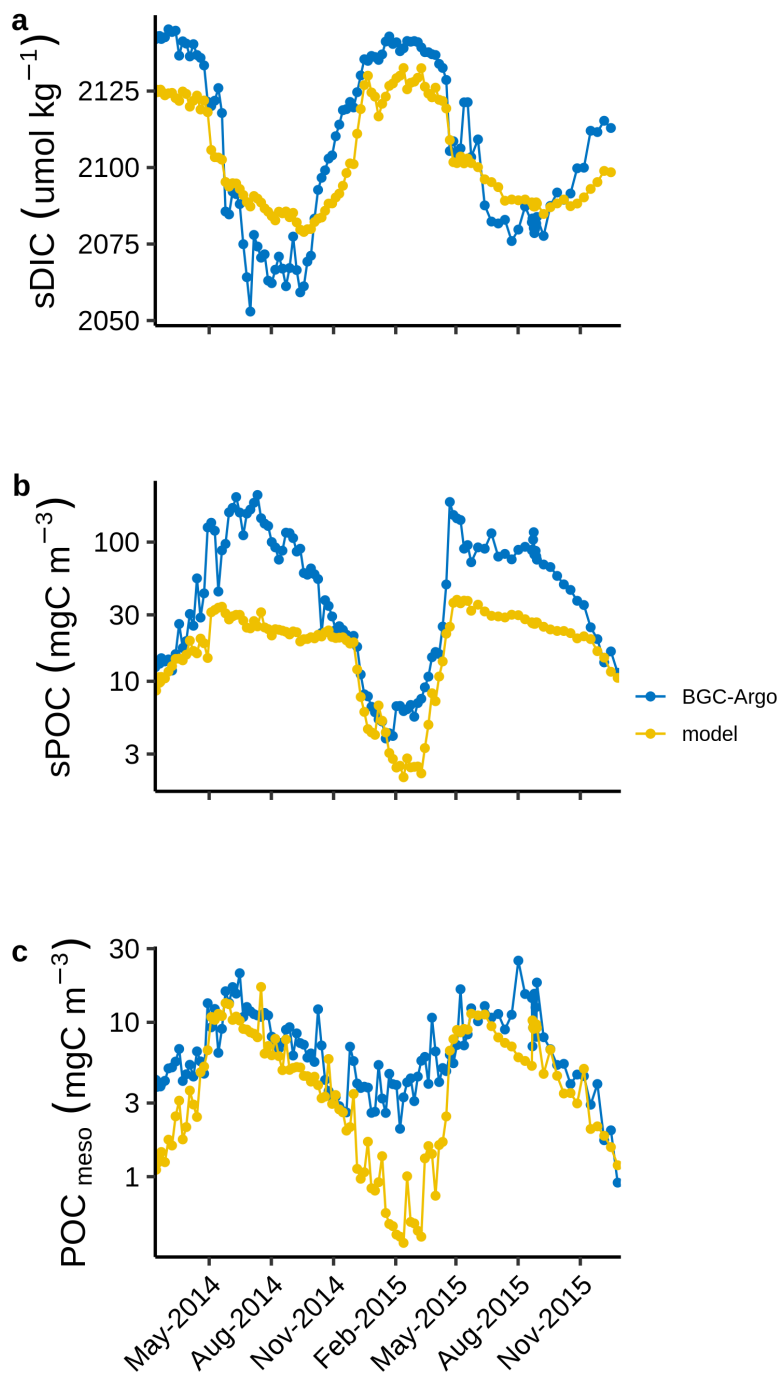
1  
2 **Figure 4.** Spatial distribution maps of BGC-Argo floats' observations of sChl (a), model sChl  
3 (b), the BIAS (c) and the RMSD (d). The data are averaged in 4°x4° bins. Bins containing  
4 less than 4 points are excluded. The BIAS and RMSD are computed on the log<sub>10</sub>-transformed  
5 data to account that sChl covers several orders of magnitude and is lognormally distributed  
6 (Campbell, 1995).

7  
8



1  
2 **Figure 5.** (a) Float trajectory of the BGC-Argo float (WMO number: 5904479). 2014-2015  
3 time series of (b), mixed layer depth, (c), sChl, (d), sNO<sub>3</sub>, (e), sSi, (f), sPO<sub>4</sub>, derived from  
4 the BGC-Argo floats observations (blue) and from the model simulation (yellow). The float  
5 sChl and sNO<sub>3</sub> are calculated from the direct observations of the floats, whereas the float sSi  
6 and sPO<sub>4</sub> result from CANYON-B predictions.

7



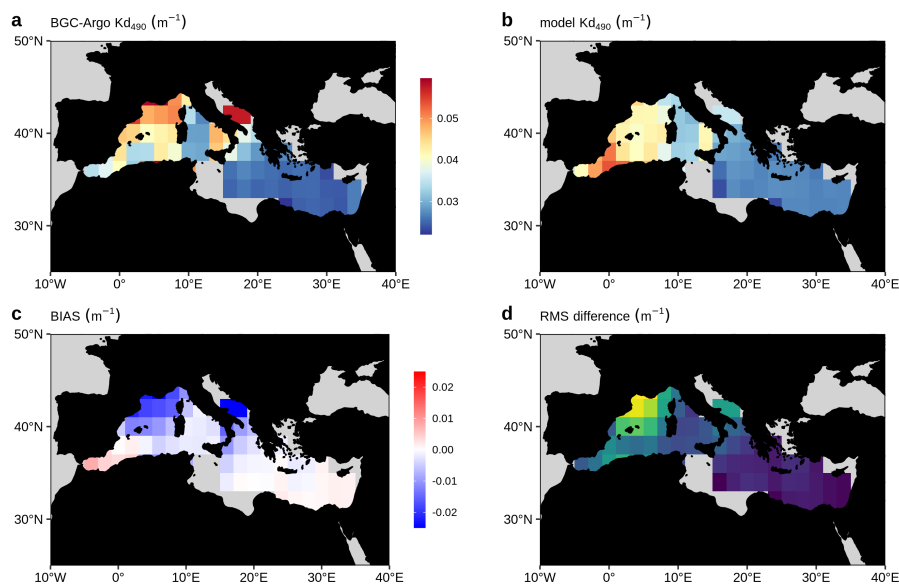
1



- 1 **Figure 6.** Same as Fig. 5 but for **(a)**, sDIC, **(b)**, sPOC, **(c)**,  $\text{POC}_{\text{meso}}$ . The float sPOC and
- 2  $\text{POC}_{\text{meso}}$  are calculated from the direct observations of the floats, whereas the float sDIC
- 3 result from CANYON-B predictions.
- 4



1



2

3 **Figure 7.** Spatial distribution maps of BGC-Argo floats' observations  $K_d$  at 490 nm (a),  
4 modelled  $K_d$  at 490 nm from the Mediterranean BGC model (b), the BIAS (c) and the RMSD  
5 (d). The data are averaged in 2°x2° bins. Bins containing less than 4 points are excluded.

6

7

8



## 1 **Appendix**

2

### 3 **A.1 The CMEMS global hydrodynamic-biogeochemical model**

4

5 The model used in this study features the offline coupled NEMO–PISCES model, with  
6 a  $1/4^\circ$  horizontal resolution 50 vertical levels (with 22 levels in the upper 100 m, the vertical  
7 resolution is 1 m near the surface and decreases to 450 m resolution near the bottom) and daily  
8 temporal resolution, covering the period from 2009 to 2017.

9

10 The biogeochemical model PISCES v2 (Aumont et al., 2015) is a model of  
11 intermediate complexity designed for global ocean applications, and is part of NEMO  
12 modelling platform. It features 24 prognostic variables and includes five nutrients that limit  
13 phytoplankton growth (nitrate, ammonium, phosphate, silicate and iron) and four living  
14 compartments: two phytoplankton size classes (nanophytoplankton and diatoms, resp. small  
15 and large) and two zooplankton size classes (microzooplankton and mesozooplankton, resp.  
16 small and large); the bacterial pool is not explicitly modelled. PISCES distinguishes three  
17 non-living detrital pools for organic carbon, particles of calcium carbonate and biogenic  
18 silicate. Additionally, the model simulates the carbonate system and dissolved oxygen.  
19 PISCES has been successfully used in a variety of biogeochemical studies, both at regional  
20 and global scale (Bopp et al., 2005; Gehlen et al., 2006, 2007; Gutknecht et al., 2019; Lefèvre  
21 et al., 2019; Schneider et al., 2008; Séférian et al., 2013; Steinacher et al., 2010; Tagliabue et  
22 al., 2010).

23

24 The dynamical component is the latest Mercator Ocean global  $1/12^\circ$  high-resolution  
25 ocean model system, extensively described and validated in Lellouche et al. (2018, 2013).  
26 This system provides daily and  $1/4^\circ$ -coarsened fields of horizontal and vertical current  
27 velocities, vertical eddy diffusivity, mixed layer depth, sea ice fraction, potential temperature,  
28 salinity, sea surface height, surface wind speed, freshwater fluxes and net surface solar  
29 shortwave irradiance that drive the transport of biogeochemical tracers. This system also  
30 features a reduced-order Kalman filter based on the Singular Evolutive Extended Kalman  
31 filter (SEEK) formulation introduced by Pham et al. (1998), that assimilates, on a 7-day  
32 assimilation cycle, along-track altimeter data, satellite Sea Surface Temperature and Sea-Ice



1 Concentration from OSTIA, and *in situ* temperature and salinity vertical profiles from the  
2 CORA 4.2 *in situ* database.

3

4 In addition, the biogeochemical component of the coupled system also embeds a  
5 reduced order Kalman filter (similar to the above mentioned) that operationally assimilates  
6 daily L4 remotely sensed surface chlorophyll  
7 ([https://resources.marine.copernicus.eu/documents/QUID/CMEMS-GLO-QUID-001-](https://resources.marine.copernicus.eu/documents/QUID/CMEMS-GLO-QUID-001-028.pdf)  
8 [028.pdf](https://resources.marine.copernicus.eu/documents/QUID/CMEMS-GLO-QUID-001-028.pdf)). In parallel, a climatological-damping is applied to nitrate, phosphate, oxygen,  
9 silicate - with World Ocean Atlas 2013 - to dissolved inorganic carbon and alkalinity – with  
10 GLODAPv2 climatology (Key et al., 2015) - and to dissolved organic carbon and iron - with a  
11 4000-year PISCES climatological run. This relaxation is set to mitigate the impact of the  
12 physical data assimilation in the offline coupled hydrodynamic-biogeochemical system,  
13 leading significant rises of nutrients in the Equatorial Belt area, and resulting in an unrealistic  
14 drift of various biogeochemical variables e.g. chlorophyll, nitrate, phosphate (Fennel et al.,  
15 2019; Park et al., 2018). The time-scale associated with this climatological damping is set to 1  
16 year and allows a smooth constraint that has been shown to be efficient to reduce the model  
17 drift.

18

## 19 **A.2 The Mediterranean Sea biogeochemical model MedBFM**

20

21 The Mediterranean Sea biogeochemical model MedBFM, is based on the system  
22 described in Teruzzi et al. (2014) and Salon et al. (2019).

23

24 The physical forcing fields needed to compute the transport include the 3-d horizontal  
25 and vertical current velocities, vertical eddy diffusivity, potential temperature, and salinity and  
26 2-d data surface data for wind stress. These forcing datasets are simulated by the Mediterranean  
27 Sea Monitoring and Forecasting Centre (MED–MFC) in the Copernicus Marine Environmental  
28 Monitoring Service (CMEMS, <http://marine.copernicus.eu>). The biogeochemical model is then  
29 offline forced adopting the output computed by the CMEMS MED-MFC. In the present  
30 application, we switched off the biogeochemical assimilation scheme that is currently used in  
31 the operational MED-MFC system.

32



1           The light propagation is resolved coupling an atmospheric multispectral radiative  
2 transfer model (Lazzari et al., 2020) with an in-water radiative model (Dutkiewicz et al., 2015)  
3 featuring bands at 25 nm resolution in the UV and visible wavelengths.

4

5           The horizontal resolution is approximately 6 km and there are 72 vertical levels with 3  
6 m resolution at surface coarsening at 300 m for the deeper layers. The biogeochemical model  
7 here adopted (Biogeochemical Flux Model -- BFM -- ; (Vichi et al., 2015)) has been already  
8 applied to simulate primary producers biogeochemistry (Lazzari et al., 2012), alkalinity spatial  
9 and temporal variability (Cossarini et al., 2015), and CO<sub>2</sub> fluxes (Canu et al., 2015) for the  
10 Mediterranean Sea, and has been corroborated using *in situ* data for the operational purposes  
11 within CMEMS (Salon et al., 2019). The BFM model has been expanded in the present  
12 configuration adding the dynamics of coloured dissolved organic carbon (CDOM) by assuming  
13 a constant CDOM:DOC production ratio (i.e. 2%, as in (Dutkiewicz et al., 2015)). The  
14 absorption of CDOM, is described using reference absorption at 450 nm of 0.015 m<sup>2</sup>/mgC  
15 (Dutkiewicz et al., 2015) and an exponential slope of 0.017 nm<sup>-1</sup> (Babin et al., 2003; Organelli  
16 et al., 2014).

17

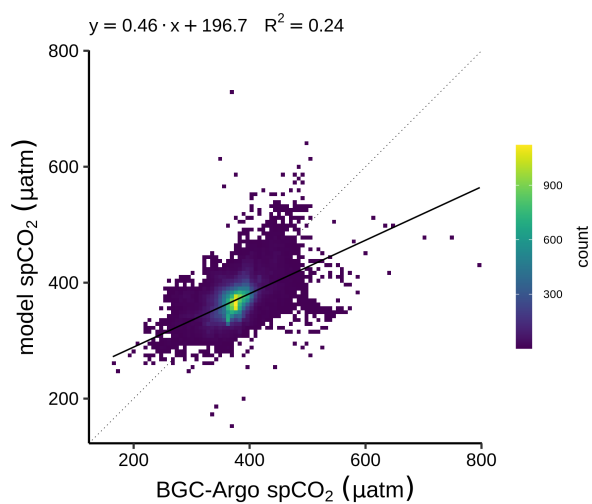
### 18 **A.3 BGC-Argo K<sub>d</sub> estimates**

19

20           The data used to compute the K<sub>d</sub> metrics are quality checked according to Organelli et  
21 al. (2017). Moreover, for the K<sub>d</sub> logarithmic interpolation, the following selection rules were  
22 applied: the profile must have at least 5 BGC Argo float sampling in the first optical depth, the  
23 gap between the two shallower acquisitions must be less than 10 meters, and there must be at  
24 least one measurement deeper than 15 meters.

25

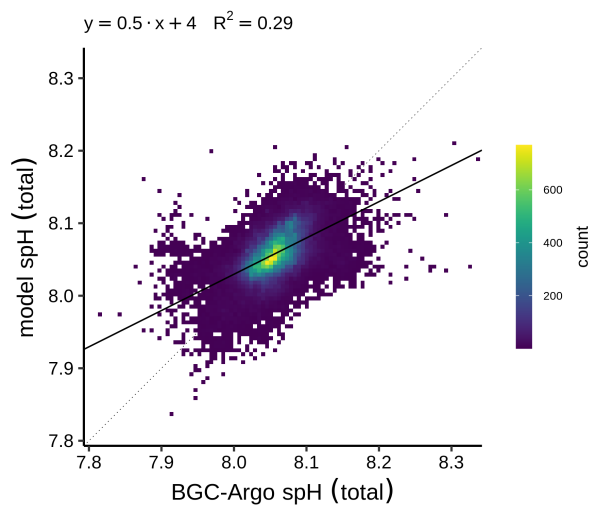
### 26 **A.4 Figures**



1

2 **Figure A1.** Same as Figure 3 but for spCO<sub>2</sub>.

3



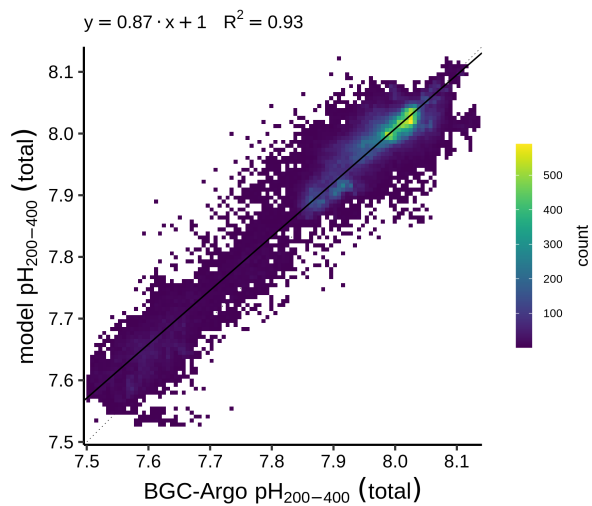
4

5 **Figure A2.** Same as Figure 3 but for spH. Note that spH is calculated from both the direct  
6 observations of the floats and as well as the estimations from CANYON-B.

7



1

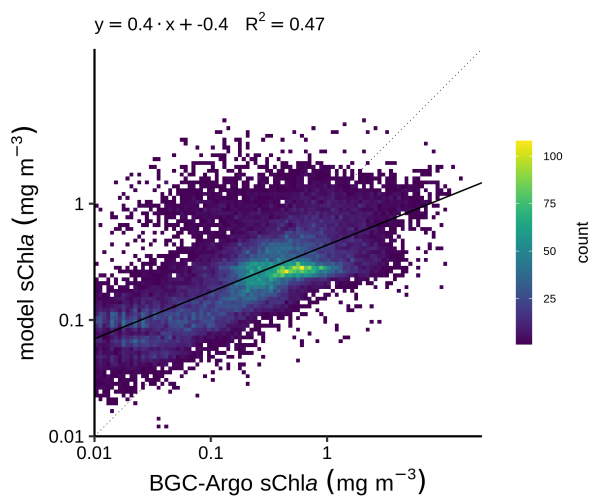


2

3 **Figure A3.** Same as Figure 3 but for pH<sub>200-400</sub>. Note that pH<sub>200-400</sub> is calculated from both the  
4 direct observations of the floats and as well as the estimations from CANYON-B.

5

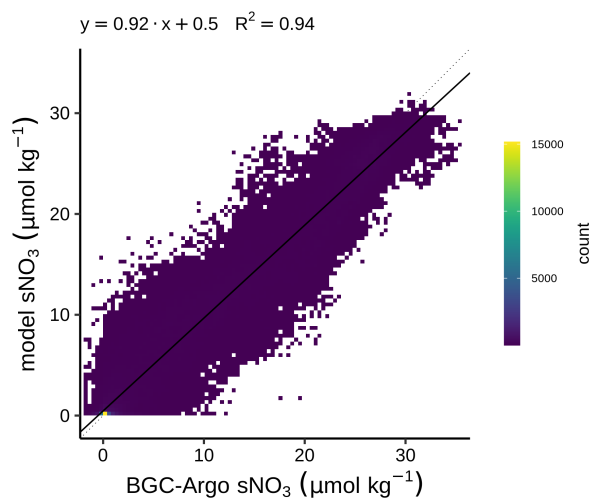
6



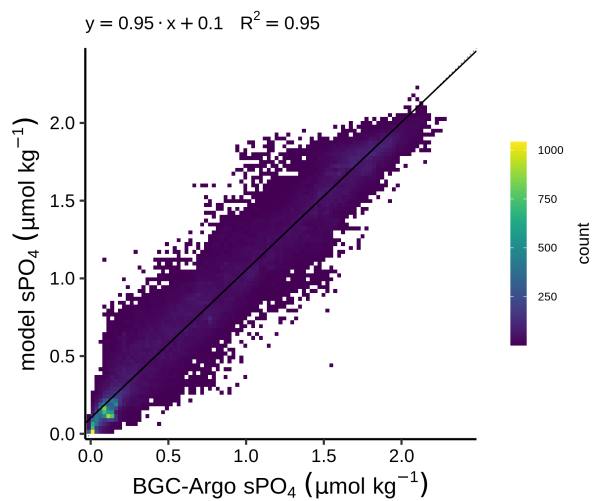
7



- 1 **Figure A4.** Same as Figure 3 but for sChl. Note that the least squares regression is computed
- 2 on the  $\log_{10}$ -transformed data to account that sChl covers several orders of magnitude and it is
- 3 lognormally distributed (Campbell, 1995). Data lower than  $0.01 \text{ mg m}^{-3}$  are not included.
- 4



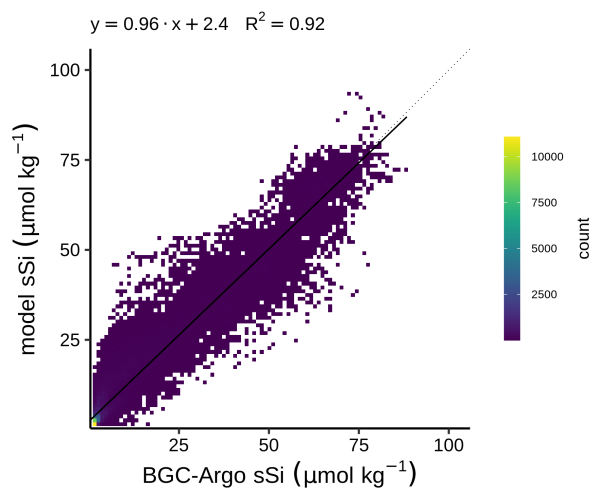
- 5
- 6 **Figure A5.** Same as Figure 3 but for  $\text{sNO}_3$ . Note that  $\text{sNO}_3$  is calculated from both the direct
- 7 observations of the floats and as well as the estimations from CANYON-B.
- 8
- 9



1

2 **Figure A6.** Same as Figure 3 but for sPO<sub>4</sub>.

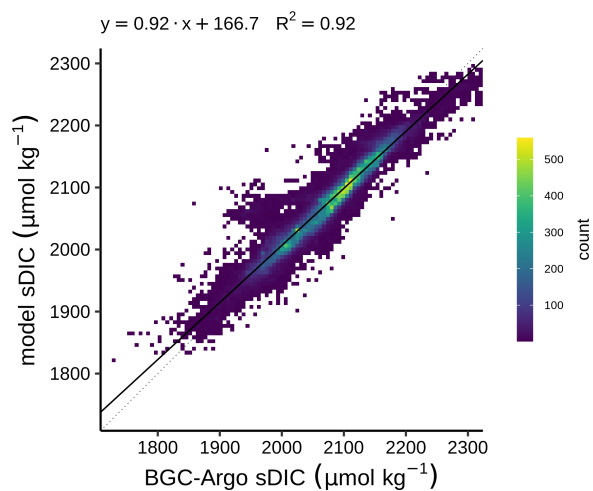
3



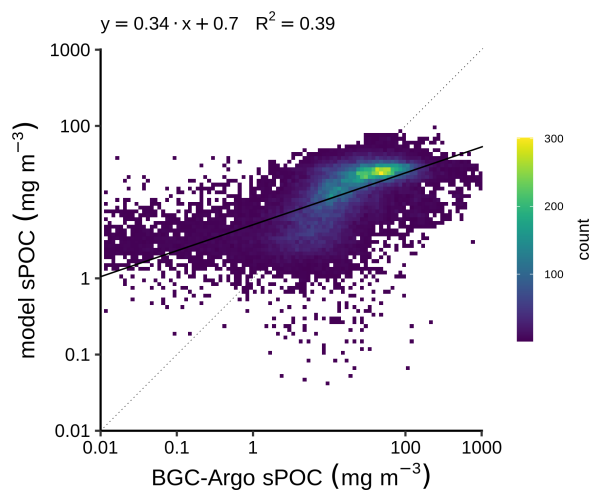
4

5 **Figure A7.** Same as Figure 3 but for sSi.

6



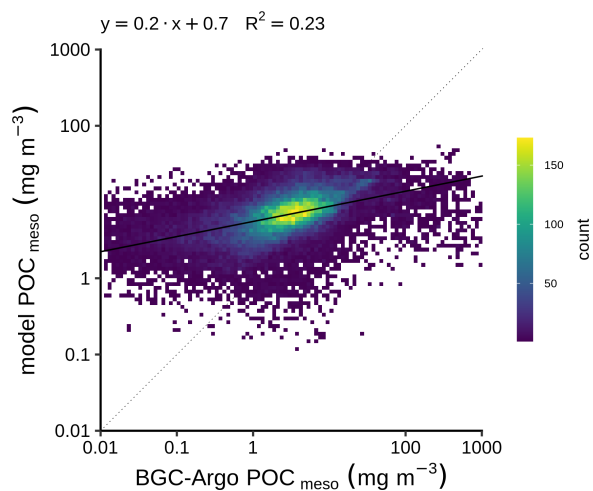
1  
2 **Figure A8.** Same as Figure 3 but for sDIC.  
3  
4



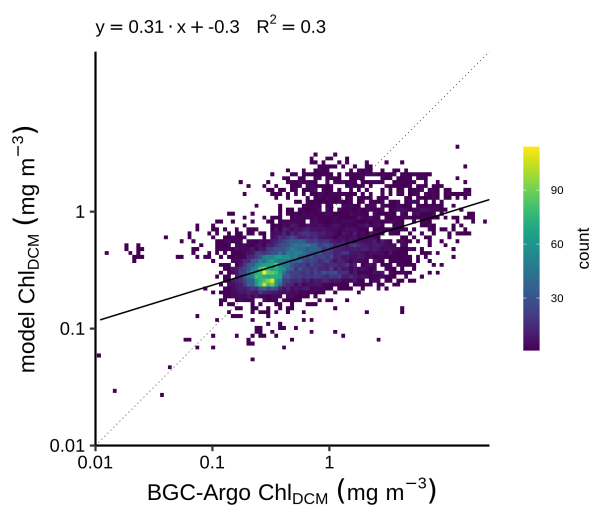
5  
6 **Figure A9.** Same as Figure 3 but for sPOC. Note that the least squares regression is  
7 computed on the  $\log_{10}$ -transformed data to account that sPOC covers several orders of



- 1 magnitude and it is lognormally distributed (Campbell, 1995). Data lower than  $0.01 \text{ mg m}^{-3}$
- 2 are not included.
- 3

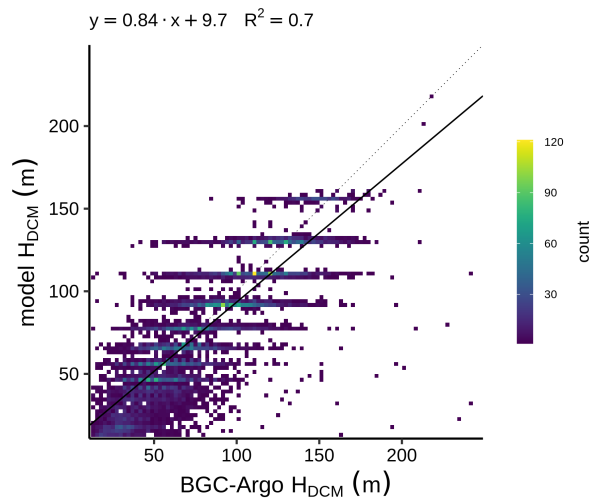


- 4
- 5 **Figure A10.** Same as Figure 3 but for POC<sub>meso</sub>. Note that the least squares regression is
- 6 computed on the log<sub>10</sub>-transformed data to account that POC<sub>meso</sub> covers several orders of
- 7 magnitude and it is lognormally distributed (Campbell, 1995). Data lower than  $0.01 \text{ mg m}^{-3}$
- 8 are not included.
- 9
- 10
- 11

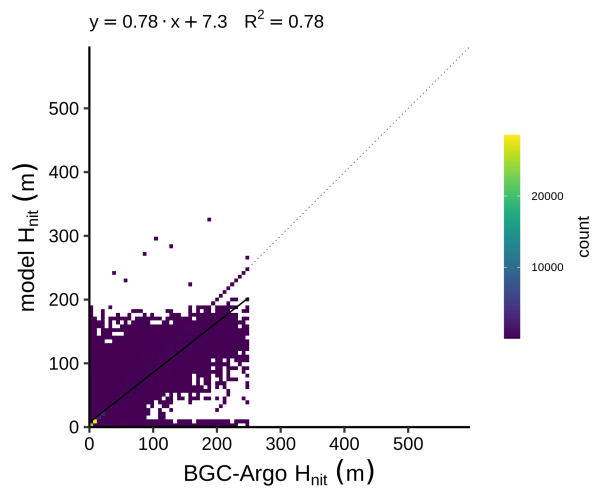


1  
2  
3  
4  
5  
6  
7  
8

**Figure A11.** Same as Figure 3 but for Chl<sub>DCM</sub>. Note that the least squares regression is computed on the log<sub>10</sub>-transformed data to account that Chl<sub>DCM</sub> covers several orders of magnitude and it is lognormally distributed (Campbell, 1995). Data lower than 0.01 mg m<sup>-3</sup> are not included. Observed DCMs deeper than 250 m are not included.



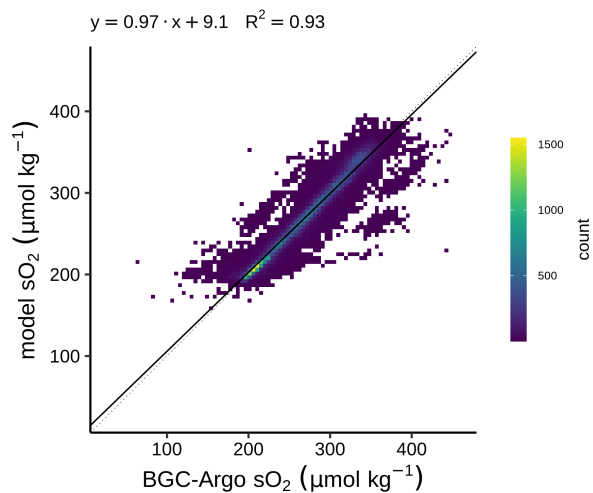
1  
2 **Figure A12.** Same as Figure 3 but for  $H_{DCM}$ . Observed DCMs deeper than 250 m are not  
3 included.



4  
5 **Figure A13.** Same as Figure 3 but for  $H_{nit}$ . Observed nitracline deeper than 250 m are not  
6 included.  
7



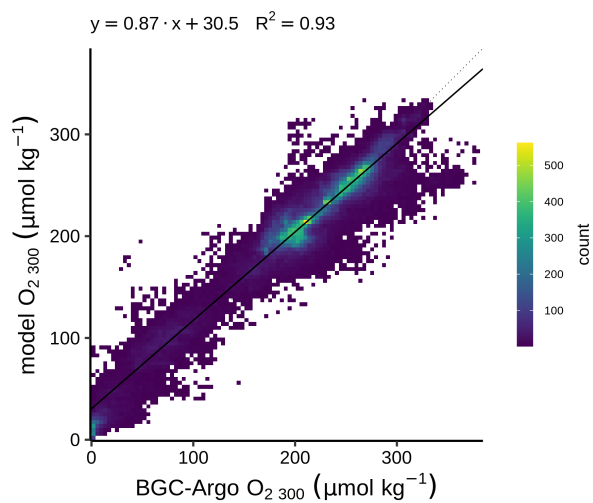
1



2

3 **Figure A14.** Same as Figure 3 but for  $sO_2$ .

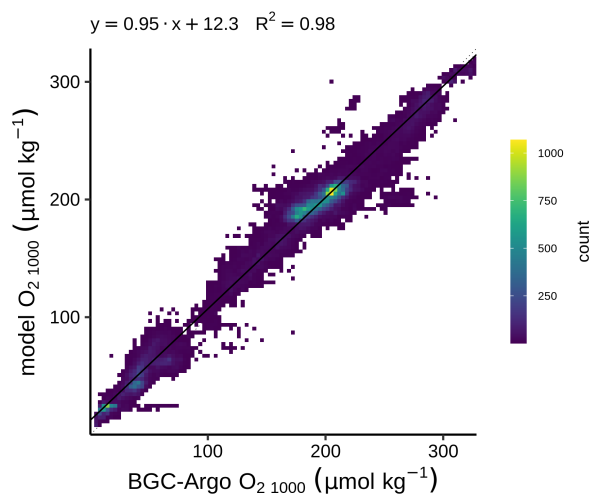
4



5

6 **Figure A15.** Same as Figure 3 but for  $O_{2\ 300}$ .

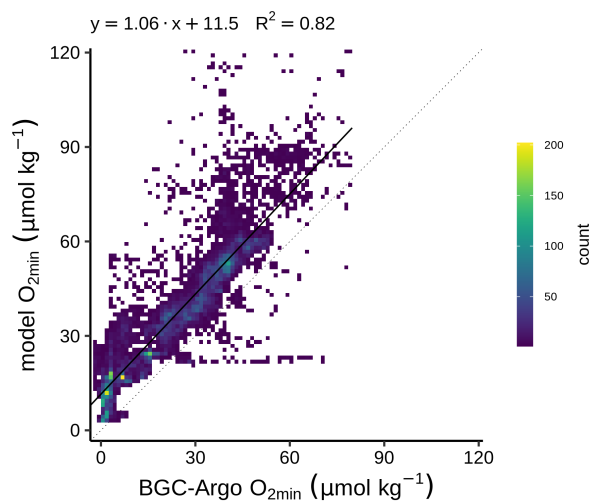
7



1

2 **Figure A16.** Same as Figure 3 but for  $O_{2,1000}$ .

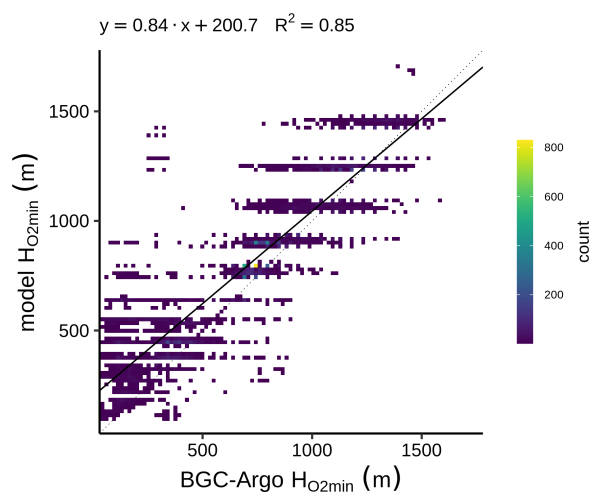
3



4

5 **Figure A17.** Same as Figure 3..

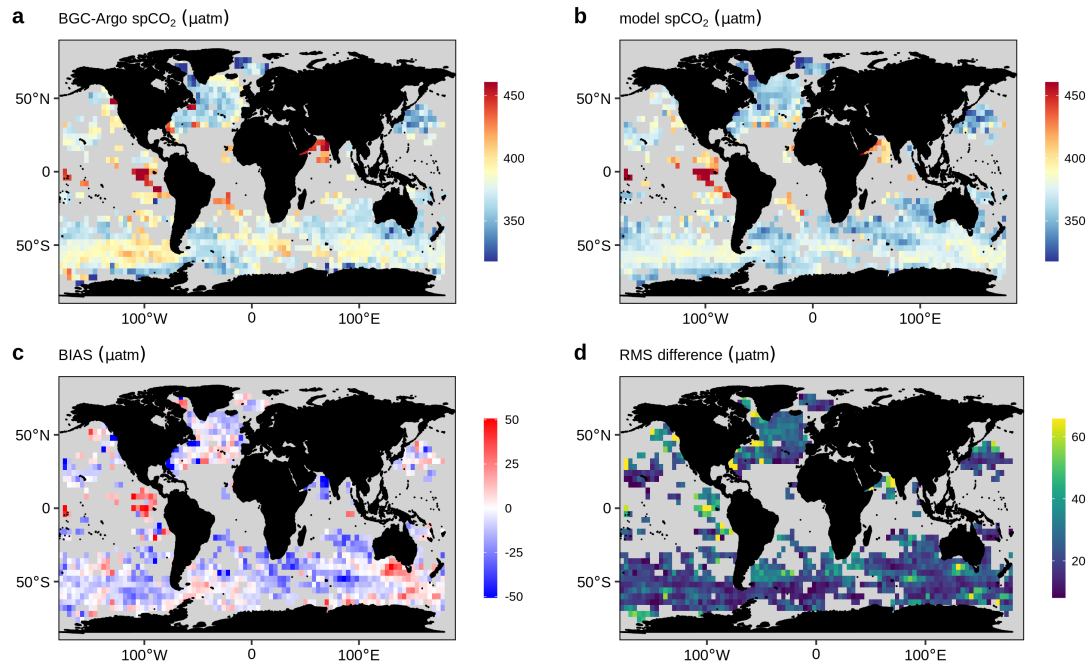
6



1  
2 **Figure A18.** Same as Figure 3 but for  $H_{O_2min}$ .  
3



1



2

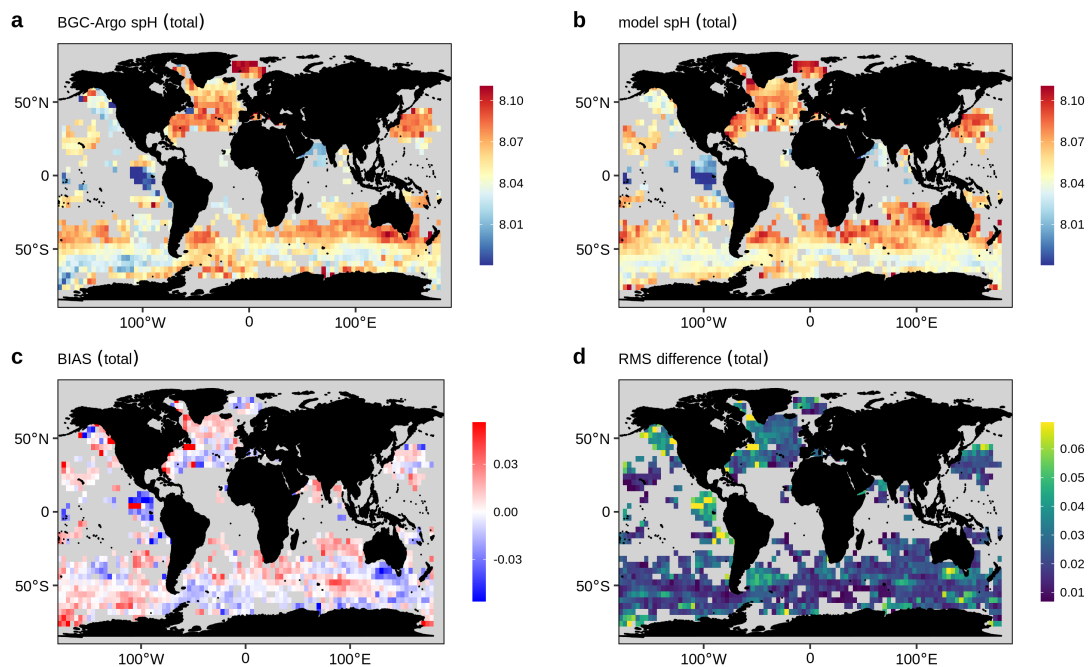
3

**Figure A19.** Same as Figure 4 but for spCO<sub>2</sub>.

4

5

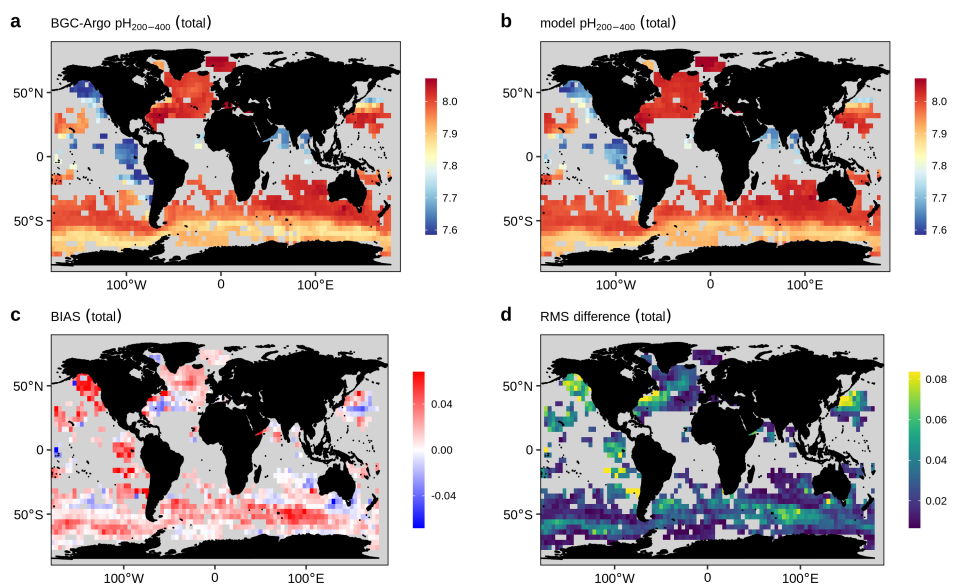
6



1

2 **Figure A20.** Same as Figure 4 but for spH. Note that spH is calculated from both the direct  
3 observations of the floats and as well as the estimations from CANYON-B.

4



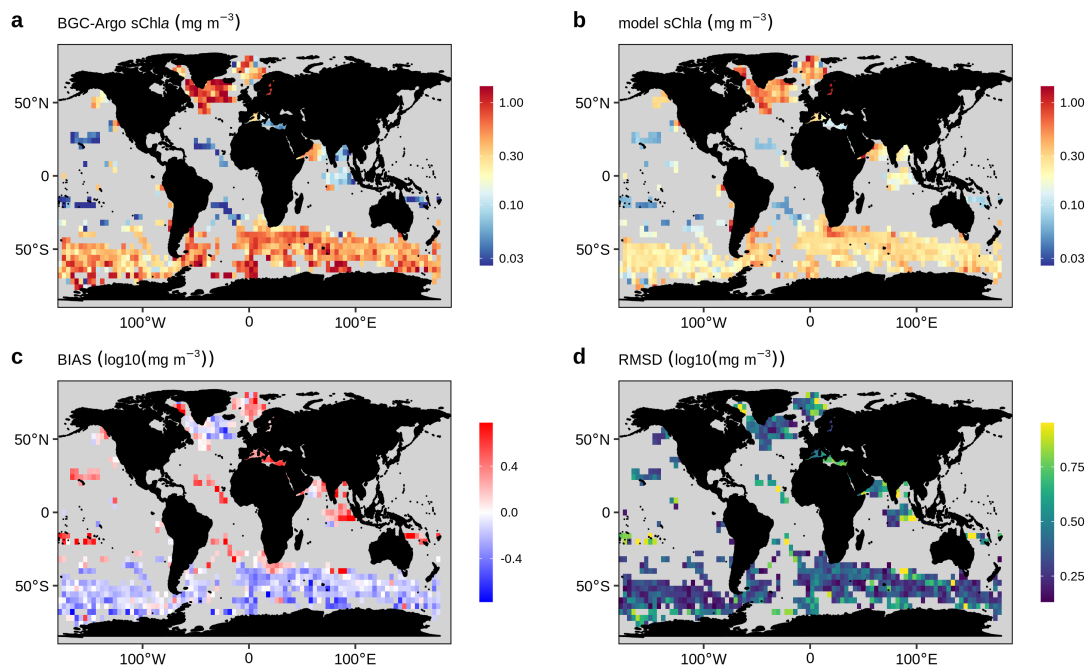
5



1 **Figure A21.** Same as Figure 4 but for  $\text{pH}_{200-400}$ . Note that  $\text{pH}_{200-400}$  is calculated from both the  
2 direct observations of the floats and as well as the estimations from CANYON-B.

3

4



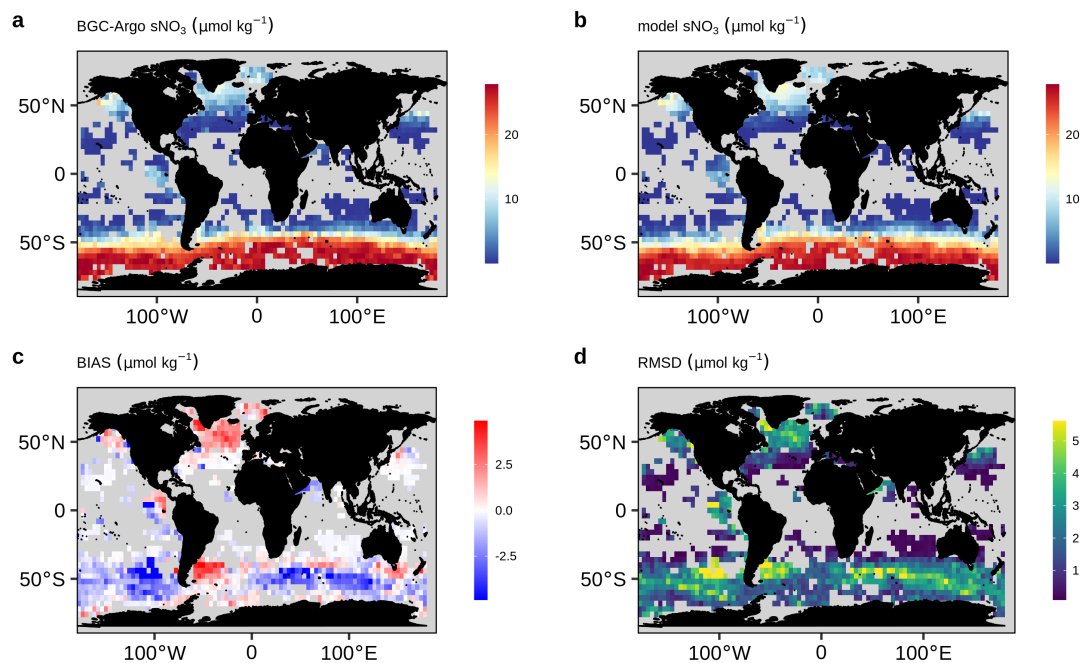
5

6 **Figure A22.** Same as Figure 4.

7

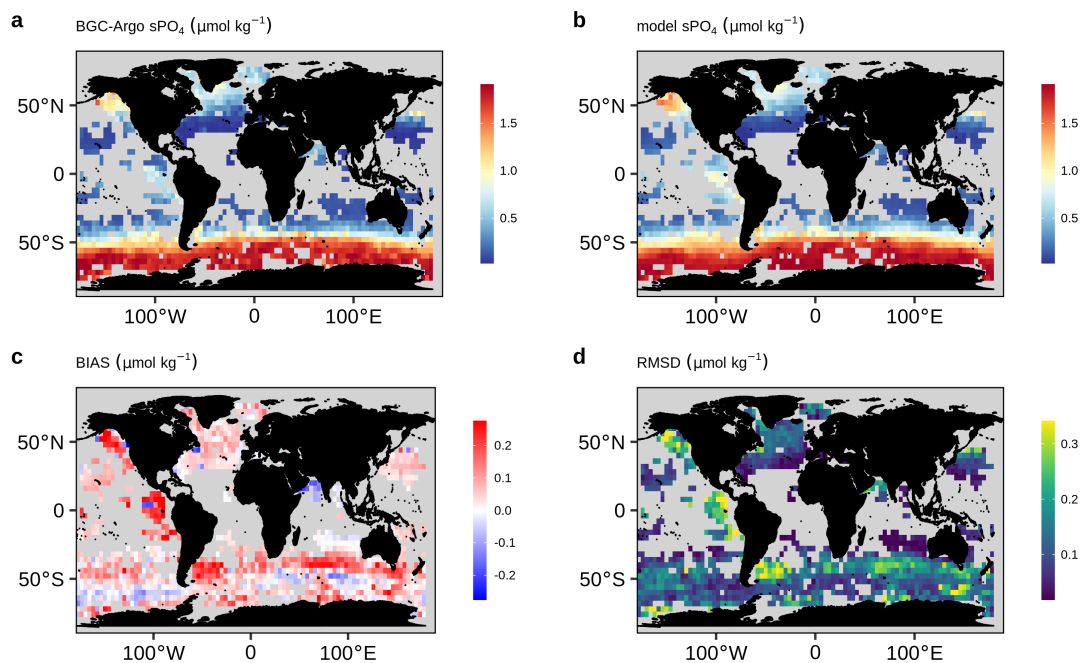
8

9



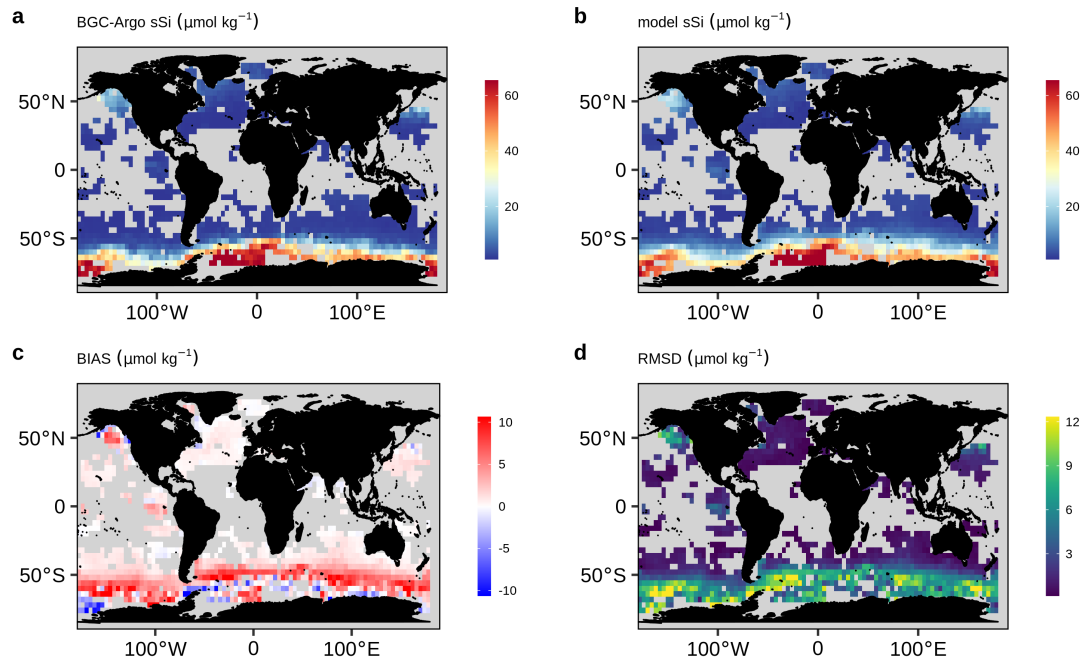
1  
2  
3  
4  
5  
6  
7

**Figure A23.** Same as Figure 4 but for sNO<sub>3</sub>. Note that sNO<sub>3</sub> is calculated from both the direct observations of the floats and as well as the estimations from CANYON-B.



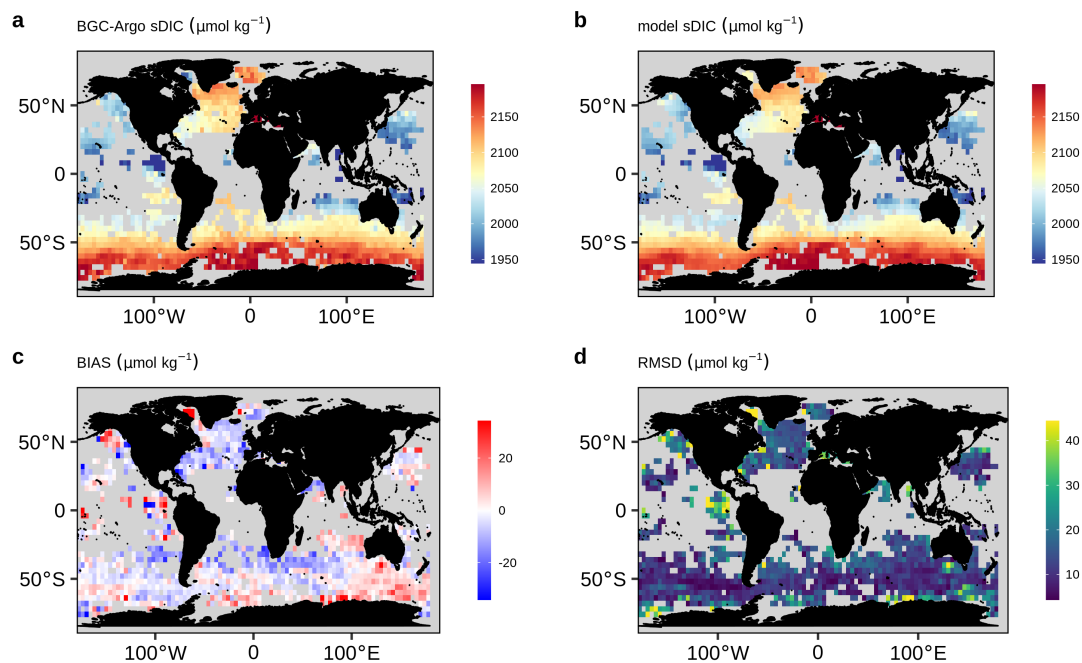
1  
2  
3  
4  
5  
6  
7

**Figure A24.** Same as Figure 4 but for  $s\text{PO}_4$ .



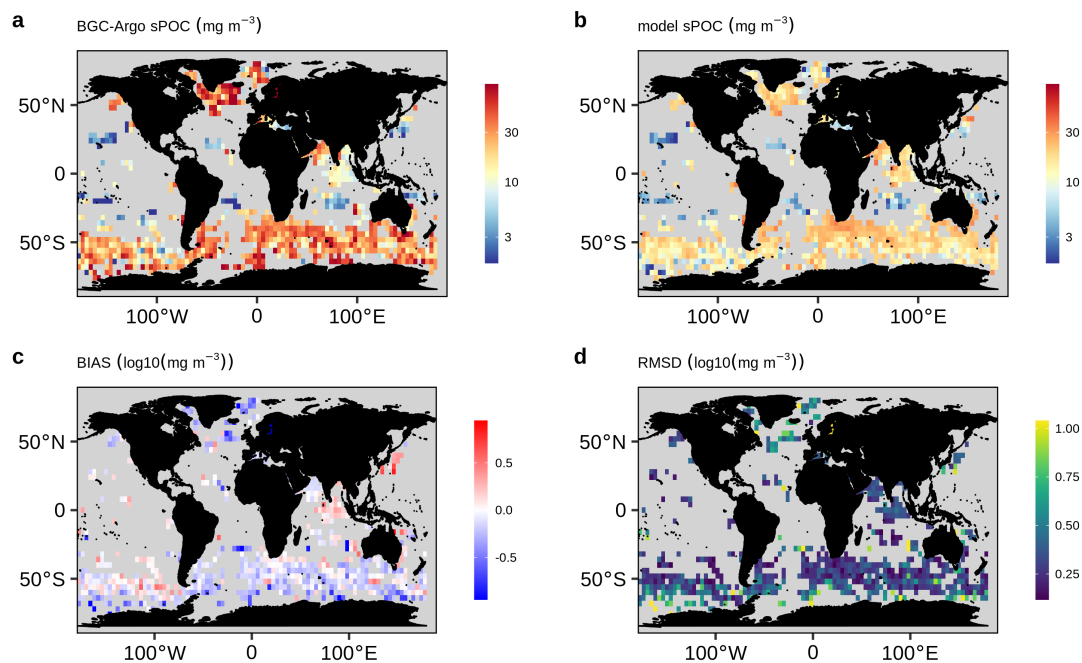
1  
2  
3  
4  
5  
6  
7  
8  
9  
10

**Figure A25.** Same as Figure 4 but for sSi.



1  
2  
3  
4  
5  
6

**Figure A26.** Same as Figure 4 but for sDIC.

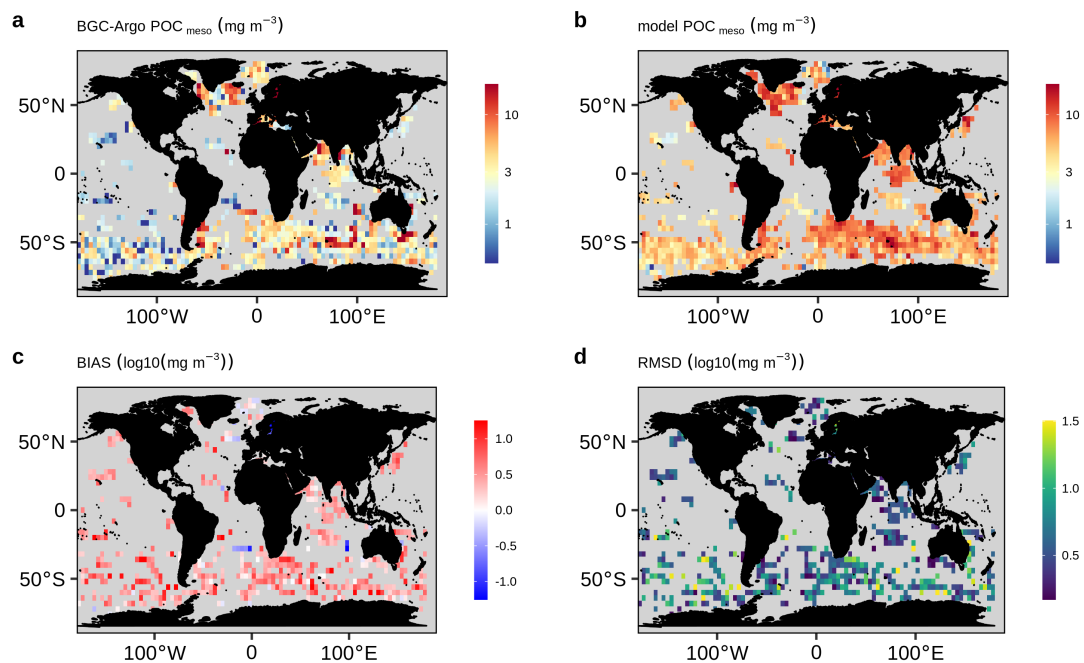


1

2 **Figure A27.** Same as Figure 4 but for sPOC. The BIAS and RMSD are computed on the  
3  $\log_{10}$ -transformed data to account that sPOC covers several orders of magnitude and it is  
4 lognormally distributed (Campbell, 1995)

5

6

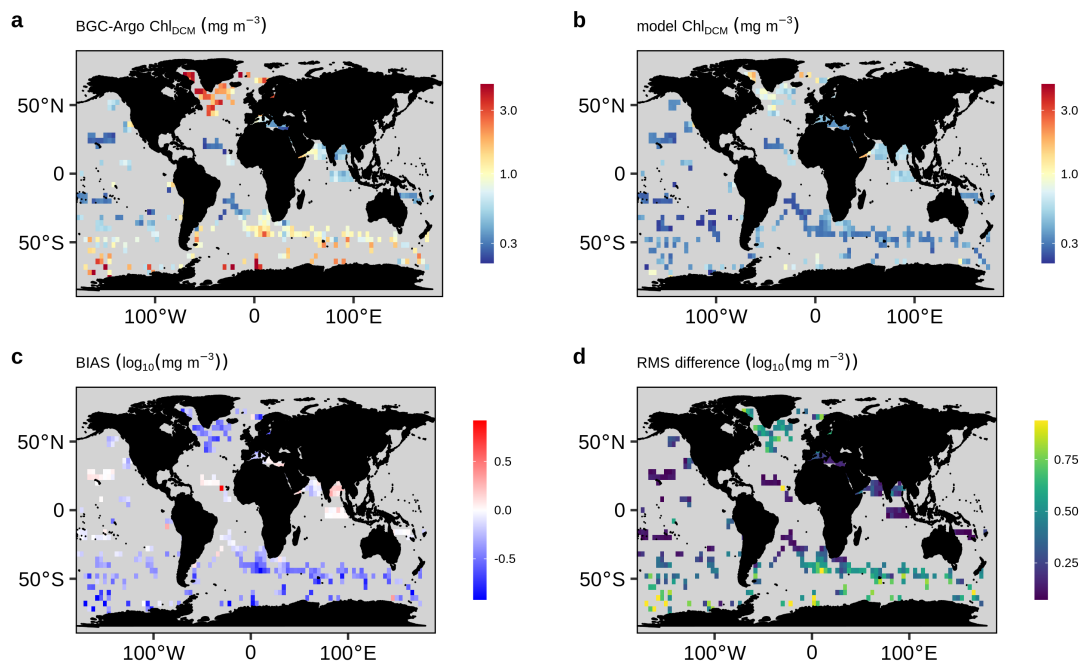


1

2 **Figure A28.** Same as Figure 4 but for POC<sub>meso</sub>. The BIAS and RMSD are computed on the  
3 log<sub>10</sub>-transformed data to account that POC<sub>meso</sub> covers several orders of magnitude and it is  
4 lognormally distributed (Campbell, 1995)

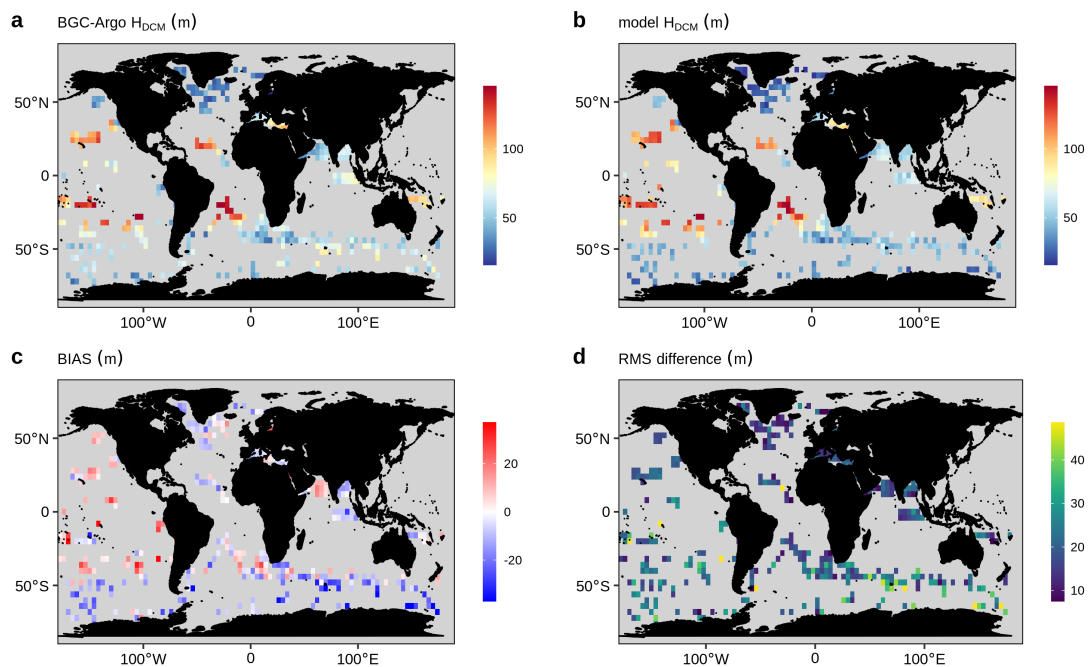
5

6



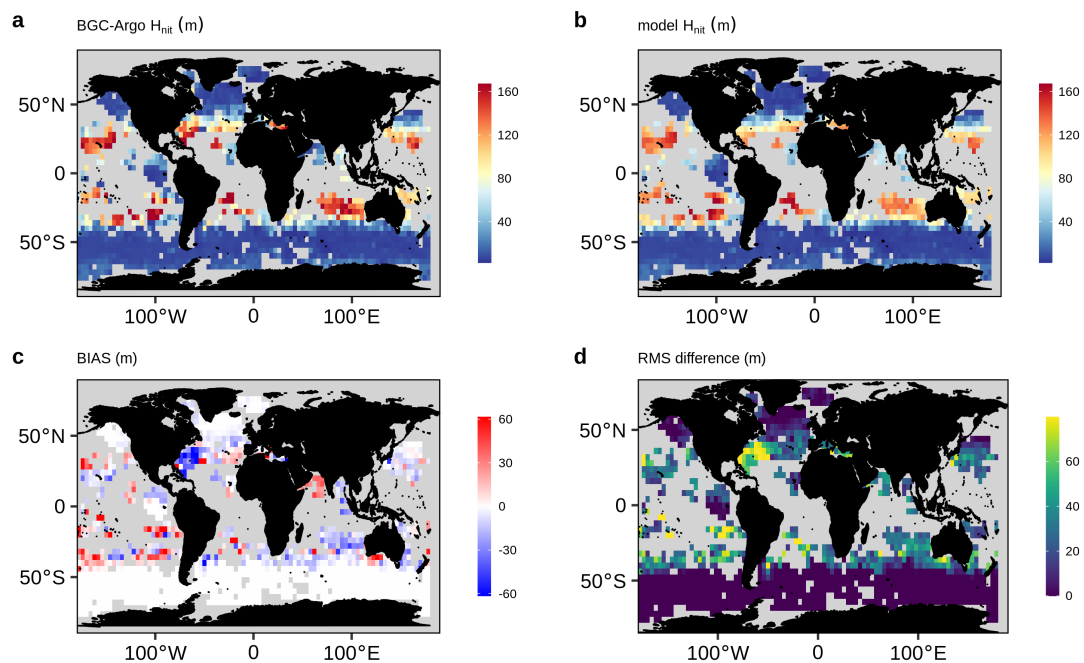
1  
2  
3  
4  
5  
6  
7  
8  
9

**Figure A29.** Same as Figure 4 but for Chl<sub>DCM</sub>. Note that the BIAS and RMSD are computed on the log<sub>10</sub>-transformed data to account that Chl<sub>DCM</sub> covers several orders of magnitude and it is lognormally distributed (Campbell, 1995).



1  
2  
3  
4  
5  
6

**Figure A30.** Same as Figure 4 but for  $H_{DCM}$ . Observed DCMs deeper than 250 m are not included.

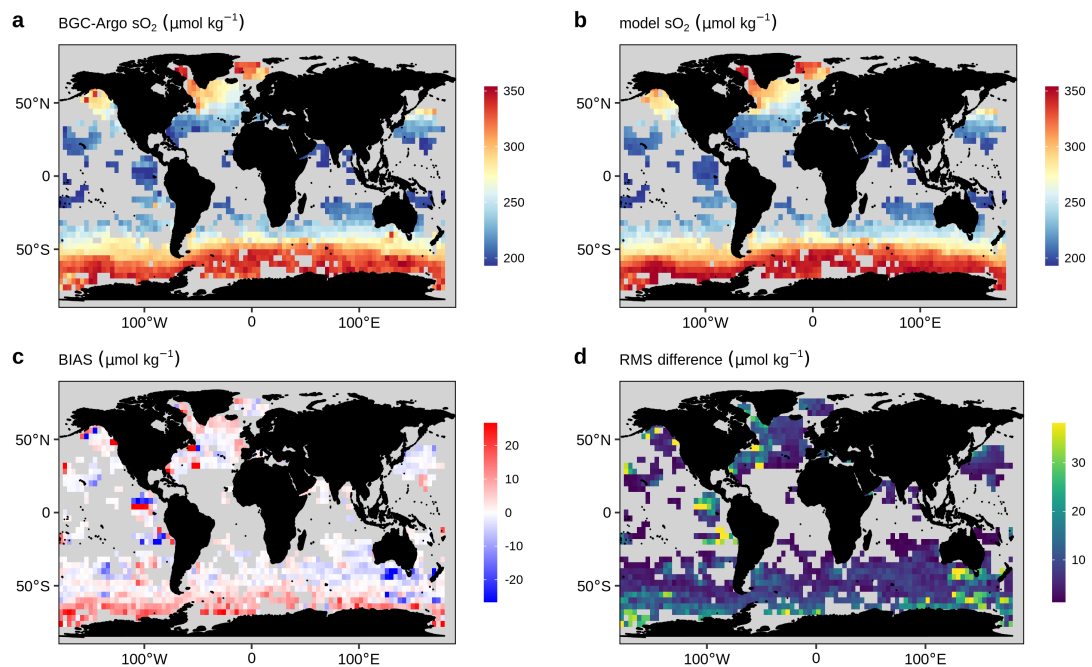


1

2 **Figure A31.** Same as Figure 4 but for  $H_{nit}$ . Observed nitracline deeper than 250 m are not  
3 included.

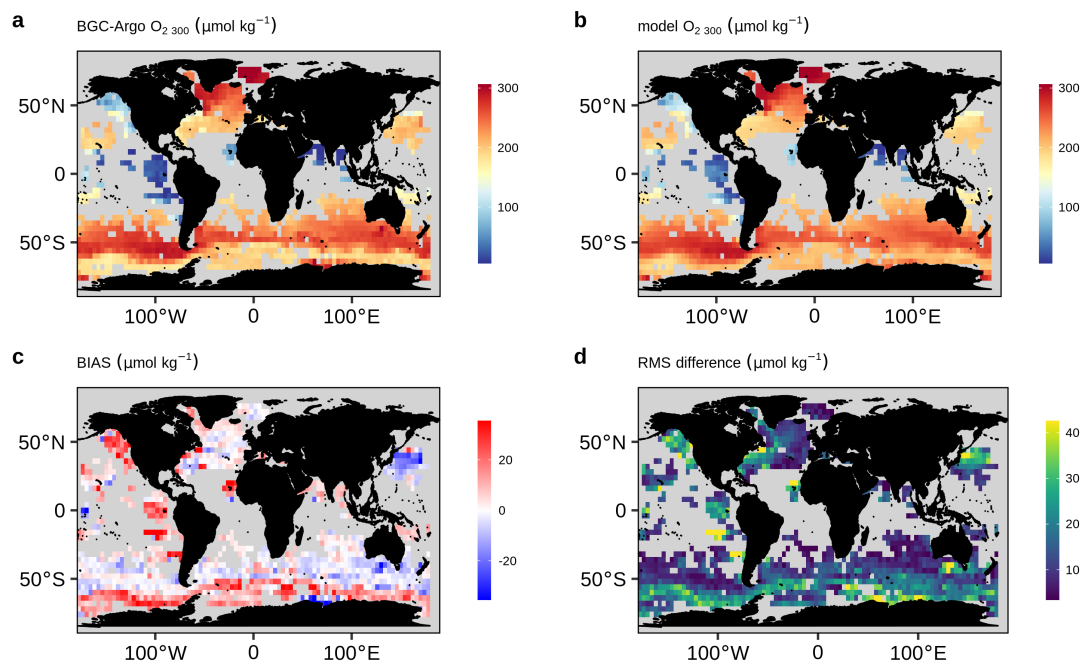
4

5



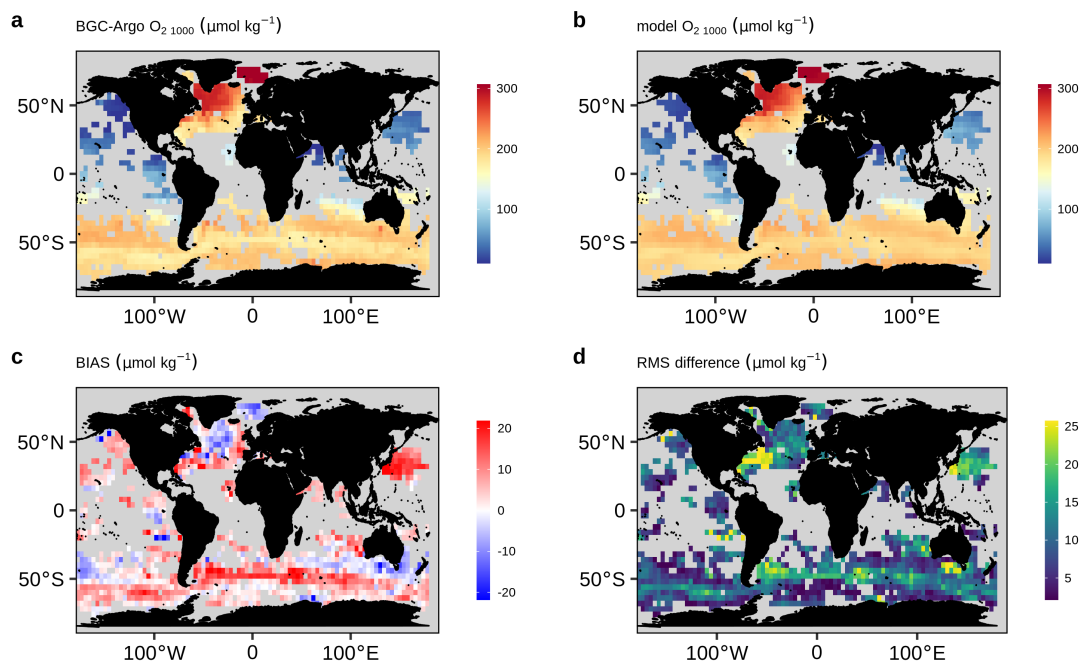
1  
2  
3  
4  
5  
6  
7

**Figure A32.** Same as Figure 4 but for  $sO_2$ .



1  
2  
3  
4  
5  
6  
7

**Figure A33.** Same as Figure 4 but for  $O_{2\ 300}$ .



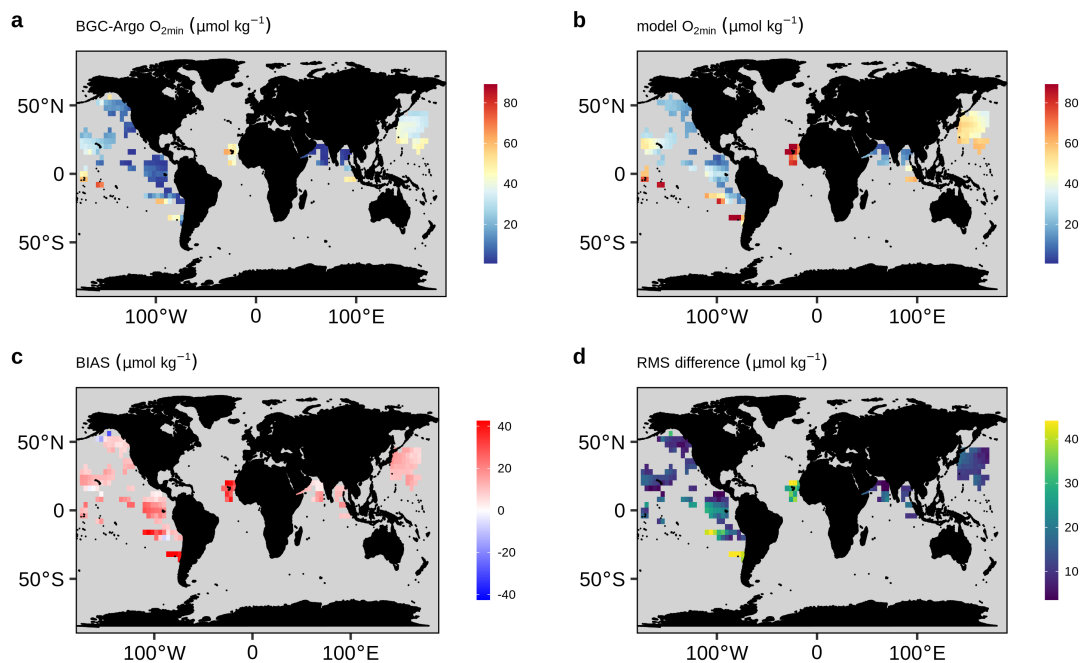
1

2 **Figure A34.** Same as Figure 4 but for O<sub>2</sub> 1000.

3

4

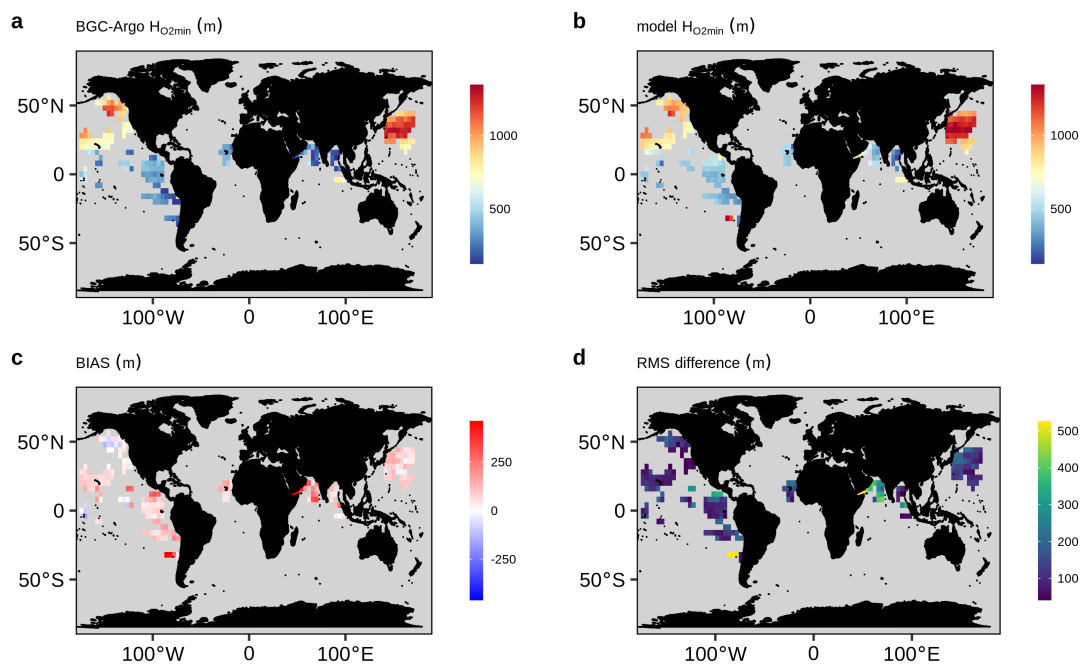
5



1

2 **Figure A35.** Same as Figure 4 but for  $O_{2min}$ .

3



4

5 **Figure A36.** Same as Figure 4 but for  $H_{2min}$ .



1 **Data availability.** The BGC model data can be downloaded from the Copernicus Marine  
2 Environmental Monitoring Service  
3 ([https://resources.marine.copernicus.eu/?option=com\\_csw&view=details&product\\_id=GLOB](https://resources.marine.copernicus.eu/?option=com_csw&view=details&product_id=GLOB)  
4 [AL\\_ANALYSIS\\_FORECAST\\_BIO\\_001\\_028](https://resources.marine.copernicus.eu/?option=com_csw&view=details&product_id=GLOB)). The BGC-Argo data were downloaded from  
5 the Argo Global Data Assembly Centre in France (<ftp://ftp.ifremer.fr/argo/>).  
6  
7 **Authors Contribution:** AM, GC, FD, SS and VT originated the study. AM, HC, FD, RS and  
8 VT designated the study. AM and RS process the BGC-Argo floats data. PL processed the  
9 BGC-Argo float in the Mediterranean Sea and run the Mediterranean BGC model. AM  
10 analysed the data. AM wrote the first draft of the manuscript. HC, GC, FD, EG, PL, CP,  
11 SS,RS,VT and AT contributed to the subsequent drafts. All authors read and approved the  
12 final draft.  
13  
14 **Competing Interests:** The authors declare no competing financial interests.  
15  
16 **Materials and correspondence:** Correspondence and request for material should be  
17 addressed to [mignot@mercator-ocean.fr](mailto:mignot@mercator-ocean.fr)  
18  
19 **Acknowledgements:** This study has been conducted using the Copernicus Marine Service  
20 products (CMEMS). The BGC-Argo data were collected and made freely available by the  
21 International Argo program and the national programs that contribute to it  
22 (<https://www.argo.jcommops.org>). The Argo program is part of the Global Ocean Observing  
23 System. Part of this work was performed within the framework of the BIOOPTIMOD and  
24 MASSIMILI CMEMS Service Evolution Projects. This paper represents a contribution to the  
25 following research projects: NAOS (funded by the Agence Nationale de la Recherche in the  
26 framework of the French “Equipement d’avenir” program, grant ANR J11R107-F), remOcean  
27 (funded by the European Research Council, grant 246777), and the French Bio-Argo program  
28 (BGC-Argo France; funded by CNES-TOSCA, LEFE-GMMC).  
29  
30



## 1 References

2

- 3 Aumont, O., Ethé, C., Tagliabue, A., Bopp, L. and Gehlen, M.: PISCES-v2: an ocean  
4 biogeochemical model for carbon and ecosystem studies, *Geosci. Model Dev.*, 8(8), 2465–  
5 2513, <https://doi.org/10.5194/gmd-8-2465-2015>, 2015.
- 6 Babin, M., Stramski, D., Ferrari, G. M., Claustre, H., Bricaud, A., Obolensky, G. and  
7 Hoepffner, N.: Variations in the light absorption coefficients of phytoplankton, nonalgal  
8 particles, and dissolved organic matter in coastal waters around Europe, *J. Geophys. Res.*  
9 *Oceans*, 108(C7), 2003.
- 10 Baird, M. E., Cherukuru, N., Jones, E., Margvelashvili, N., Mongin, M., Oubelkheir, K.,  
11 Ralph, P. J., Rizwi, F., Robson, B. J., Schroeder, T., Skerratt, J., Steven, A. D. L. and Wild-  
12 Allen, K. A.: Remote-sensing reflectance and true colour produced by a coupled  
13 hydrodynamic, optical, sediment, biogeochemical model of the Great Barrier Reef, Australia:  
14 Comparison with satellite data, *Environ. Model. Softw.*, 78, 79–96,  
15 <https://doi.org/10.1016/j.envsoft.2015.11.025>, 2016.
- 16 Barbieux, M., Uitz, J., Gentili, B., Pasqueron de Fommervault, O., Mignot, A., Poteau, A.,  
17 Schmechtig, C., Taillandier, V., Leymarie, E., Penker&apos;h, C.,  
18 D&apos;Ortenzio, F., Claustre, H. and Bricaud, A.: Bio-optical characterization of  
19 subsurface chlorophyll maxima in the Mediterranean Sea from a Biogeochemical-Argo float  
20 database, *Biogeosciences*, 16(6), 1321–1342, <https://doi.org/10.5194/bg-16-1321-2019>, 2019.
- 21 Biogeochemical-Argo Planning Group: The scientific rationale, design and implementation  
22 plan for a Biogeochemical-Argo float array., 2016.
- 23 Bittig, H. C., Steinhoff, T., Claustre, H., Fiedler, B., Williams, N. L., Sauzède, R., Körtzinger,  
24 A. and Gattuso, J.-P.: An alternative to static climatologies: robust estimation of open ocean  
25 CO<sub>2</sub> variables and nutrient concentrations from T, S, and O<sub>2</sub> data using Bayesian neural  
26 networks, *Front. Mar. Sci.*, 5, 328, 2018.
- 27 Bittig, H. C., Maurer, T. L., Plant, J. N., Wong, A. P., Schmechtig, C., Claustre, H., Trull, T.  
28 W., Udaya Bhaskar, T. V. S., Boss, E. and Dall’Olmo, G.: A BGC-Argo guide: Planning,  
29 deployment, data handling and usage, *Front. Mar. Sci.*, 6, 502, 2019.
- 30 Bopp, L., Aumont, O., Cadule, P., Alvain, S. and Gehlen, M.: Response of diatoms  
31 distribution to global warming and potential implications: A global model study, *Geophys.*  
32 *Res. Lett.*, 32(19), <https://doi.org/10.1029/2005GL023653>, 2005.
- 33 Bosc, E., Bricaud, A. and Antoine, D.: Seasonal and interannual variability in algal biomass  
34 and primary production in the Mediterranean Sea, as derived from 4 years of SeaWiFS  
35 observations, *Glob. Biogeochem. Cycles*, 18(1), <https://doi.org/10.1029/2003GB002034>,  
36 2004.
- 37 Breitburg, D., Levin, L. A., Oschlies, A., Grégoire, M., Chavez, F. P., Conley, D. J., Garçon,  
38 V., Gilbert, D., Gutiérrez, D., Isensee, K., Jacinto, G. S., Limburg, K. E., Montes, I., Naqvi, S.  
39 W. A., Pitcher, G. C., Rabalais, N. N., Roman, M. R., Rose, K. A., Seibel, B. A., Telszewski,



- 1 M., Yasuhara, M. and Zhang, J.: Declining oxygen in the global ocean and coastal waters,  
2 Science, 359(6371), <https://doi.org/10.1126/science.aam7240>, 2018.
- 3 Briggs, N., Perry, M. J., Cetinić, I., Lee, C., D'Asaro, E., Gray, A. M. and Rehm, E.: High-  
4 resolution observations of aggregate flux during a sub-polar North Atlantic spring bloom,  
5 Deep Sea Res. Part Oceanogr. Res. Pap., 58(10), 1031–1039,  
6 <https://doi.org/10.1016/j.dsr.2011.07.007>, 2011.
- 7 Campbell, J. W.: The lognormal distribution as a model for bio-optical variability in the sea,  
8 J. Geophys. Res. Oceans, 100(C7), 13237–13254, <https://doi.org/10.1029/95JC00458>, 1995.
- 9 Canu, D. M., Ghermandi, A., Nunes, P. A., Lazzari, P., Cossarini, G. and Solidoro, C.:  
10 Estimating the value of carbon sequestration ecosystem services in the Mediterranean Sea: An  
11 ecological economics approach, Glob. Environ. Change, 32, 87–95, 2015.
- 12 Capuzzo, E., Lynam, C. P., Barry, J., Stephens, D., Forster, R. M., Greenwood, N.,  
13 McQuatters-Gollop, A., Silva, T., van Leeuwen, S. M. and Engelhard, G. H.: A decline in  
14 primary production in the North Sea over 25 years, associated with reductions in zooplankton  
15 abundance and fish stock recruitment, Glob. Change Biol., 24(1), e352–e364,  
16 <https://doi.org/10.1111/gcb.13916>, 2018.
- 17 Cetinic, I., Perry, M. J., Briggs, N. T., Kallin, E., D'Asaro, E. A. and Lee, C. M.: Particulate  
18 organic carbon and inherent optical properties during 2008 North Atlantic Bloom  
19 Experiment, J. Geophys. Res.-Oceans, 117, <https://doi.org/10.1029/2011JC007771>, 2012.
- 20 Claustre, H., Johnson, K. S. and Takeshita, Y.: Observing the Global Ocean with  
21 Biogeochemical-Argo, Annu. Rev. Mar. Sci., 12(1), annurev-marine-010419-010956,  
22 <https://doi.org/10.1146/annurev-marine-010419-010956>, 2020.
- 23 Cossarini, G., Lazzari, P. and Solidoro, C.: Spatiotemporal variability of alkalinity in the  
24 Mediterranean Sea, Biogeosciences, 12(6), 1647–1658, [https://doi.org/10.5194/bg-12-1647-](https://doi.org/10.5194/bg-12-1647-2015)  
25 2015, 2015.
- 26 Cossarini, G., Mariotti, L., Feudale, L., Mignot, A., Salon, S., Taillandier, V., Teruzzi, A. and  
27 D'Ortenzio, F.: Towards operational 3D-Var assimilation of chlorophyll Biogeochemical-  
28 Argo float data into a biogeochemical model of the Mediterranean Sea, Ocean Model., 133,  
29 112–128, <https://doi.org/10.1016/j.ocemod.2018.11.005>, 2019.
- 30 Crowder, L. B., Hazen, E. L., Avissar, N., Bjorkland, R., Latanich, C. and Ogburn, M. B.:  
31 The Impacts of Fisheries on Marine Ecosystems and the Transition to Ecosystem-Based  
32 Management, Annu. Rev. Ecol. Evol. Syst., 39(1), 259–278,  
33 <https://doi.org/10.1146/annurev.ecolsys.39.110707.173406>, 2008.
- 34 Cullen, J. J.: Subsurface Chlorophyll Maximum Layers: Enduring Enigma or Mystery  
35 Solved?, Annu. Rev. Mar. Sci., 7(1), 207–239, [https://doi.org/10.1146/annurev-marine-](https://doi.org/10.1146/annurev-marine-010213-135111)  
36 010213-135111, 2015.
- 37 Dale, T., Rey, F. and Heimdal, B. R.: Seasonal development of phytoplankton at a high  
38 latitude oceanic site, Sarsia, 84(5–6), 419–435, 1999.
- 39 Dall'Olmo, G. and Mork, K. A.: Carbon export by small particles in the Norwegian Sea,  
40 Geophys. Res. Lett., 41(8), 2921–2927, <https://doi.org/10.1002/2014GL059244>, 2014.



- 1 Doney, S. C., Lima, I., Moore, J. K., Lindsay, K., Behrenfeld, M. J., Westberry, T. K.,  
2 Mahowald, N., Glover, D. M. and Takahashi, T.: Skill metrics for confronting global upper  
3 ocean ecosystem-biogeochemistry models against field and remote sensing data, *J. Mar. Syst.*,  
4 76(1), 95–112, <https://doi.org/10.1016/j.jmarsys.2008.05.015>, 2009.
- 5 D’Ortenzio, F., Lavigne, H., Besson, F., Claustre, H., Coppola, L., Garcia, N., Laes-Huon, A.,  
6 Le Reste, S., Malarde, D., Migon, C., Morin, P., Mortier, L., Poteau, A., Prieur, L.,  
7 Raimbault, P. and Testor, P.: Observing mixed layer depth, nitrate and chlorophyll  
8 concentrations in the northwestern Mediterranean: A combined satellite and NO<sub>3</sub> profiling  
9 floats experiment, *Geophys. Res. Lett.*, 41(18), 2014GL061020,  
10 <https://doi.org/10.1002/2014GL061020>, 2014.
- 11 Dutkiewicz, S., Hickman, A. E., Jahn, O., Gregg, W. W., Mouw, C. B. and Follows, M. J.:  
12 Capturing optically important constituents and properties in a marine biogeochemical and  
13 ecosystem model, *Biogeosciences*, 12(14), 4447–4481, [https://doi.org/10.5194/bg-12-4447-](https://doi.org/10.5194/bg-12-4447-2015)  
14 2015, 2015.
- 15 Eriksen, M., Lebreton, L. C. M., Carson, H. S., Thiel, M., Moore, C. J., Borerro, J. C.,  
16 Galgani, F., Ryan, P. G. and Reisser, J.: Plastic Pollution in the World’s Oceans: More than 5  
17 Trillion Plastic Pieces Weighing over 250,000 Tons Afloat at Sea, edited by H. G. Dam, *PLoS*  
18 *ONE*, 9(12), e111913, <https://doi.org/10.1371/journal.pone.0111913>, 2014.
- 19 Evans, G. T. and Parslow, J. S.: A Model of Annual Plankton Cycles, *Biol. Oceanogr.*, 3(3),  
20 327–347, <https://doi.org/10.1080/01965581.1985.10749478>, 1985.
- 21 Fennel, K., Gehlen, M., Brasseur, P., Brown, C. W., Ciavatta, S., Cossarini, G., Crise, A.,  
22 Edwards, C. A., Ford, D., Friedrichs, M. A. M., Gregoire, M., Jones, E., Kim, H.-C.,  
23 Lamouroux, J., Murtugudde, R., Perruche, C. and the GODAE OceanView Marine Ecosystem  
24 Analysis and Prediction Task Team: Advancing Marine Biogeochemical and Ecosystem  
25 Reanalyses and Forecasts as Tools for Monitoring and Managing Ecosystem Health, *Front.*  
26 *Mar. Sci.*, 6, 89, <https://doi.org/10.3389/fmars.2019.00089>, 2019.
- 27 Ford, D.: Assimilating synthetic Biogeochemical-Argo and ocean colour observations into a  
28 global ocean model to inform observing system design, preprint, *Biogeochemistry: Open*  
29 *Ocean.*, 2020.
- 30 Friedlingstein, P., Jones, M. W., O’Sullivan, M., Andrew, R. M., Hauck, J., Peters, G. P.,  
31 Peters, W., Pongratz, J., Sitch, S., Le Quéré, C., Bakker, D. C. E., Canadell, J. G., Ciais, P.,  
32 Jackson, R. B., Anthoni, P., Barbero, L., Bastos, A., Bastrikov, V., Becker, M., Bopp, L.,  
33 Buitenhuis, E., Chandra, N., Chevallier, F., Chini, L. P., Currie, K. I., Feely, R. A., Gehlen,  
34 M., Gilfillan, D., Gkritzalis, T., Goll, D. S., Gruber, N., Gutekunst, S., Harris, I., Haverd, V.,  
35 Houghton, R. A., Hurtt, G., Ilyina, T., Jain, A. K., Joetzjer, E., Kaplan, J. O., Kato, E., Klein  
36 Goldewijk, K., Korsbakken, J. I., Landschützer, P., Lauvset, S. K., Lefèvre, N., Lenton, A.,  
37 Lienert, S., Lombardozi, D., Marland, G., McGuire, P. C., Melton, J. R., Metzl, N., Munro,  
38 D. R., Nabel, J. E. M. S., Nakaoka, S.-I., Neill, C., Omar, A. M., Ono, T., Peregon, A.,  
39 Pierrot, D., Poulter, B., Rehder, G., Resplandy, L., Robertson, E., Rödenbeck, C., Séférian,  
40 R., Schwinger, J., Smith, N., Tans, P. P., Tian, H., Tilbrook, B., Tubiello, F. N., van der Werf,  
41 G. R., Wiltshire, A. J. and Zaehle, S.: Global Carbon Budget 2019, *Earth Syst. Sci. Data*,  
42 11(4), 1783–1838, <https://doi.org/10.5194/essd-11-1783-2019>, 2019.



- 1 Gehlen, M., Bopp, L., Emprin, N., Aumont, O., Heinze, C. and Ragueneau, O.: Reconciling  
2 surface ocean productivity, export fluxes and sediment composition in a global  
3 biogeochemical ocean model, *Biogeosciences*, 3(4), 521–537, [https://doi.org/10.5194/bg-3-](https://doi.org/10.5194/bg-3-521-2006)  
4 521-2006, 2006.
- 5 Gehlen, M., Gangstø, R., Schneider, B., Bopp, L., Aumont, O. and Ethe, C.: The fate of  
6 pelagic CaCO<sub>3</sub> production in a high CO<sub>2</sub> ocean: a model study, *Biogeosciences*, 4(4), 505–  
7 519, <https://doi.org/10.5194/bg-4-505-2007>, 2007.
- 8 Gittings, J. A., Raitsos, D. E., Kheireddine, M., Racault, M.-F., Claustre, H. and Hoteit, I.:  
9 Evaluating tropical phytoplankton phenology metrics using contemporary tools, *Sci. Rep.*,  
10 9(1), 1–9, 2019.
- 11 Gregg, W. W. and Rousseaux, C. S.: Directional and spectral irradiance in ocean models:  
12 effects on simulated global phytoplankton, nutrients, and primary production, *Front. Mar.*  
13 *Sci.*, 3, 240, 2016.
- 14 Gutknecht, E., Reffray, G., Mignot, A., Dabrowski, T. and Sotillo, M. G.: Modelling the  
15 marine ecosystem of Iberia-Biscay-Ireland (IBI) European waters for CMEMS operational  
16 applications, *Ocean Sci.*, 15(6), 1489–1516, <https://doi.org/10.5194/os-15-1489-2019>, 2019.
- 17 Herbland, A. and Voituriez, B.: Hydrological structure analysis for estimating the primary  
18 production in the tropical Atlantic Ocean, *J Mar Res*, 37(1), 87–101, 1979.
- 19 Iida, Y., Takatani, Y., Kojima, A. and Ishii, M.: Global trends of ocean CO<sub>2</sub> sink and ocean  
20 acidification: an observation-based reconstruction of surface ocean inorganic carbon  
21 variables, *J. Oceanogr.*, 1–36, 2020.
- 22 Johnson, Plant, J. N., Coletti, L. J., Jannasch, H. W., Sakamoto, C. M., Riser, S. C., Swift, D.  
23 D., Williams, N. L., Boss, E., Haëntjens, N., Talley, L. D. and Sarmiento, J. L.:  
24 Biogeochemical sensor performance in the SOCCOM profiling float array: SOCCOM  
25 BIOGEOCHEMICAL SENSOR PERFORMANCE, *J. Geophys. Res. Oceans*, 122(8), 6416–  
26 6436, <https://doi.org/10.1002/2017JC012838>, 2017.
- 27 Johnson, Plant, J. N. and Maurer, T. L.: Processing BGC-Argo pH data at the DAC level,  
28 <https://archimer.ifremer.fr/doc/00460/57195/>, last access: 22 April 2020a, 2018.
- 29 Johnson, Pasquero De Fommervault, O., Serra, R., D’Ortenzio, F., Schmechtig, C., Claustre,  
30 H. and Poteau, A.: Processing Bio-Argo nitrate concentration at the DAC Level,  
31 <https://archimer.ifremer.fr/doc/00350/46121/>, last access: 22 April 2020b, 2018.
- 32 Key, R. M., Olsen, A., van Heuven, S., Lauvset, S. K., Velo, A., Lin, X., Schirnick, C.,  
33 Kozyr, A., Tanhua, T. and Hoppema, M.: Global Ocean Data Analysis Project, Version 2  
34 (GLODAPv2), Carbon Dioxide Information Analysis Center, Oak Ridge Nat Lab., 2015.
- 35 Kwiatkowski, L., Torres, O., Bopp, L., Aumont, O., Chamberlain, M., Christian, J. R., Dunne,  
36 J. P., Gehlen, M., Ilyina, T., John, J. G., Lenton, A., Li, H., Lovenduski, N. S., Orr, J. C.,  
37 Palmieri, J., Santana-Falcón, Y., Schwinger, J., Séférian, R., Stock, C. A., Tagliabue, A.,  
38 Takano, Y., Tjiputra, J., Toyama, K., Tsujino, H., Watanabe, M., Yamamoto, A., Yool, A.  
39 and Ziehn, T.: Twenty-first century ocean warming, acidification, deoxygenation, and upper-  
40 ocean nutrient and primary production decline from CMIP6 model projections,  
41 *Biogeosciences*, 17(13), 3439–3470, <https://doi.org/10.5194/bg-17-3439-2020>, 2020.



- 1 Lazzari, Solidoro, C., Ibello, V., Salon, S., Teruzzi, A., Béranger, K., Colella, S. and Crise,  
2 A.: Seasonal and inter-annual variability of plankton chlorophyll and primary production in  
3 the Mediterranean Sea: a modelling approach, *Biogeosciences*, 9(1), 217–233,  
4 <https://doi.org/10.5194/bg-9-217-2012>, 2012.
- 5 Lazzari, Solidoro, C., Salon, S. and Bolzon, G.: Spatial variability of phosphate and nitrate in  
6 the Mediterranean Sea: A modeling approach, *Deep Sea Res. Part Oceanogr. Res. Pap.*, 108,  
7 39–52, <https://doi.org/10.1016/j.dsr.2015.12.006>, 2016.
- 8 Lazzari, Salon, S., Terzić, E., Gregg, W. W., D’Ortenzio, F., Vellucci, V., Organelli, E. and  
9 Antoine, D.: Assessment of the spectral downward irradiance at the surface of  
10 theMediterranean Sea using the OASIM ocean-atmosphere radiative model, preprint,  
11 *Surface/Numerical Models/Mediterranean Sea/Air-sea fluxes/Oceanic ecosystems.*, 2020.
- 12 Lefèvre, N., Veeda, D., Tyaquicã, P., Perruche, C., Diverrès, D. and Ibánhez, J. S. P.: Basin-  
13 Scale Estimate of the Sea-Air CO<sub>2</sub> Flux During the 2010 Warm Event in the Tropical North  
14 Atlantic, *J. Geophys. Res. Biogeosciences*, 124(4), 973–986,  
15 <https://doi.org/10.1029/2018JG004840>, 2019.
- 16 Lellouche, Greiner, E., Le Galloudec, O., Garric, G., Regnier, C., Drevillon, M., Benkiran,  
17 M., Testut, C.-E., Bourdalle-Badie, R., Gasparin, F., Hernandez, O., Levier, B., Drillet, Y.,  
18 Remy, E. and Le Traon, P.-Y.: Recent updates to the Copernicus Marine Service global ocean  
19 monitoring and forecasting real-time 1/12° high-resolution system, *Ocean Sci.*, 14(5), 1093–  
20 1126, <https://doi.org/10.5194/os-14-1093-2018>, 2018.
- 21 Lellouche, J.-M., Le Galloudec, O., Drévillon, M., Régnier, C., Greiner, E., Garric, G., Ferry,  
22 N., Desportes, C., Testut, C.-E., Bricaud, C., Bourdallé-Badie, R., Tranchant, B., Benkiran,  
23 M., Drillet, Y., Daudin, A. and De Nicola, C.: Evaluation of global monitoring and  
24 forecasting systems at Mercator Océan, *Ocean Sci.*, 9(1), 57–81, <https://doi.org/10.5194/os-9-57-2013>, 2013.
- 26 Letelier, R. M., Karl, D. M., Abbott, M. R. and Bidigare, R. R.: Light driven seasonal patterns  
27 of chlorophyll and nitrate in the lower euphotic zone of the North Pacific Subtropical Gyre,  
28 *Limnol. Oceanogr.*, 49(2), 508–519, 2004.
- 29 Lynch, D. R., McGillicuddy, D. J. and Werner, F. E.: Skill assessment for coupled  
30 biological/physical models of marine systems, *J. Mar. Syst.*, 1(76), 1–3, 2009.
- 31 Macías, D., Stips, A. and Garcia-Gorriz, E.: The relevance of deep chlorophyll maximum in  
32 the open Mediterranean Sea evaluated through 3D hydrodynamic-biogeochemical coupled  
33 simulations, *Ecol. Model.*, 281, 26–37, 2014.
- 34 Mignot, Claustre, H., Uitz, J., Poteau, A., D’Ortenzio, F. and Xing, X.: Understanding the  
35 seasonal dynamics of phytoplankton biomass and the deep chlorophyll maximum in  
36 oligotrophic environments: A Bio-Argo float investigation, *Glob. Biogeochem. Cycles*, 28(8),  
37 856–876, <https://doi.org/10.1002/2013GB004781>, 2014.
- 38 Mignot, Ferrari, R. and Claustre, H.: Floats with bio-optical sensors reveal what processes  
39 trigger the North Atlantic bloom, *Nat. Commun.*, 9(1), <https://doi.org/10.1038/s41467-017-02143-6>, 2018.



- 1 Mignot, A., Claustre, H., D’Ortenzio, F., Xing, X., Poteau, A. and Ras, J.: From the shape of  
2 the vertical profile of in vivo fluorescence to Chlorophyll-a concentration, *Biogeosciences*,  
3 8(8), 2391–2406, <https://doi.org/10.5194/bg-8-2391-2011>, 2011.
- 4 Mignot, A., D’Ortenzio, F., Taillandier, V., Cossarini, G. and Salon, S.: Quantifying  
5 Observational Errors in Biogeochemical-Argo Oxygen, Nitrate, and Chlorophyll *a*  
6 Concentrations, *Geophys. Res. Lett.*, 46(8), 4330–4337,  
7 <https://doi.org/10.1029/2018GL080541>, 2019.
- 8 Organelli, E., Bricaud, A., Antoine, D. and Matsuoka, A.: Seasonal dynamics of light  
9 absorption by chromophoric dissolved organic matter (CDOM) in the NW Mediterranean Sea  
10 (BOUSSOLE site), *Deep Sea Res. Part Oceanogr. Res. Pap.*, 91, 72–85, 2014.
- 11 Organelli, E., Barbieux, M., Claustre, H., Schmechtig, C., Poteau, A., Bricaud, A., Boss, E.  
12 B., Briggs, N., Dall’Olmo, G. and d’Ortenzio, F.: Two databases derived from BGC-Argo  
13 float measurements for marine biogeochemical and bio-optical applications, *Earth Syst. Sci.*  
14 *Data*, 9, 861–880, 2017.
- 15 Osman, M. B., Das, S. B., Trusel, L. D., Evans, M. J., Fischer, H., Grieman, M. M., Kipfstuhl,  
16 S., McConnell, J. R. and Saltzman, E. S.: Industrial-era decline in subarctic Atlantic  
17 productivity, *Nature*, 569(7757), 551–555, <https://doi.org/10.1038/s41586-019-1181-8>, 2019.
- 18 Park, J.-Y., Stock, C. A., Yang, X., Dunne, J. P., Rosati, A., John, J. and Zhang, S.: Modeling  
19 Global Ocean Biogeochemistry With Physical Data Assimilation: A Pragmatic Solution to the  
20 Equatorial Instability, *J. Adv. Model. Earth Syst.*, 10(3), 891–906,  
21 <https://doi.org/10.1002/2017MS001223>, 2018.
- 22 Richardson, K. and Bendtsen, J.: Vertical distribution of phytoplankton and primary  
23 production in relation to nutricline depth in the open ocean, *Mar. Ecol. Prog. Ser.*, 620, 33–46,  
24 <https://doi.org/10.3354/meps12960>, 2019.
- 25 Riley, G.: Factors Controlling Phytoplankton Populations on Georges Bank, *J. Mar. Res.*,  
26 6(1), 54–73, 1946.
- 27 Roesler, C., Uitz, J., Claustre, H., Boss, E., Xing, X., Organelli, E., Briggs, N., Bricaud, A.,  
28 Schmechtig, C., Poteau, A., D’Ortenzio, F., Ras, J., Drapeau, S., Haëntjens, N. and Barbieux,  
29 M.: Recommendations for obtaining unbiased chlorophyll estimates from in situ chlorophyll  
30 fluorometers: A global analysis of WET Labs ECO sensors, *Limnol. Oceanogr. Methods*,  
31 15(6), 572–585, <https://doi.org/10.1002/lom3.10185>, 2017.
- 32 Roxy, M. K., Modi, A., Murtugudde, R., Valsala, V., Panickal, S., Prasanna Kumar, S.,  
33 Ravichandran, M., Vichi, M. and Lévy, M.: A reduction in marine primary productivity  
34 driven by rapid warming over the tropical Indian Ocean, *Geophys. Res. Lett.*, 43(2), 826–833,  
35 <https://doi.org/10.1002/2015GL066979>, 2016.
- 36 Russell, J. L., Kamenkovich, I., Bitz, C., Ferrari, R., Gille, S. T., Goodman, P. J., Hallberg,  
37 R., Johnson, K., Khazmutdinova, K. and Marinov, I.: Metrics for the evaluation of the  
38 Southern Ocean in coupled climate models and earth system models, *J. Geophys. Res.*  
39 *Oceans*, 123(5), 3120–3143, 2018.
- 40 Salon, S., Cossarini, G., Bolzon, G., Feudale, L., Lazzari, P., Teruzzi, A., Solidoro, C. and  
41 Crise, A.: Novel metrics based on Biogeochemical Argo data to improve the model



- 1 uncertainty evaluation of the CMEMS Mediterranean marine ecosystem forecasts, *Ocean Sci.*,  
2 15(4), 997–1022, <https://doi.org/10.5194/os-15-997-2019>, 2019.
- 3 Sauzède, R., Bittig, H. C., Claustre, H., Pasqueron de Fommervault, O., Gattuso, J.-P.,  
4 Legendre, L. and Johnson, K. S.: Estimates of Water-Column Nutrient Concentrations and  
5 Carbonate System Parameters in the Global Ocean: A Novel Approach Based on Neural  
6 Networks, *Front. Mar. Sci.*, 4, <https://doi.org/10.3389/fmars.2017.00128>, 2017.
- 7 Schartau, M., Wallhead, P., Hemmings, J., Löptien, U., Kriest, I., Krishna, S., Ward, B. A.,  
8 Slawig, T. and Oschlies, A.: Reviews and syntheses: parameter identification in marine  
9 planktonic ecosystem modelling, *Biogeosciences*, 14(6), 1647–1701,  
10 <https://doi.org/10.5194/bg-14-1647-2017>, 2017.
- 11 Schmechtig, C., Poteau, A., Claustre, H., D’Ortenzio, F. and Boss, E.: Processing bio-Argo  
12 chlorophyll-A concentration at the DAC level, *Ifremer.*, 2015.
- 13 Schmechtig, C., Claustre, H., Poteau, A. and D’Ortenzio, F.: Bio-Argo quality control manual  
14 for the Chlorophyll-A concentration, *Ifremer.*, 2018.
- 15 Schmidtko, S., Stramma, L. and Visbeck, M.: Decline in global oceanic oxygen content  
16 during the past five decades, *Nature*, 542(7641), 335–339,  
17 <https://doi.org/10.1038/nature21399>, 2017.
- 18 Schneider, B., Bopp, L., Gehlen, M., Segschneider, J., Frölicher, T. L., Cadule, P.,  
19 Friedlingstein, P., Doney, S. C., Behrenfeld, M. J. and Joos, F.: Climate-induced interannual  
20 variability of marine primary and export production in three global coupled climate carbon  
21 cycle models, *Biogeosciences*, 5(2), 597–614, <https://doi.org/10.5194/bg-5-597-2008>, 2008.
- 22 Sférian, R., Bopp, L., Gehlen, M., Orr, J. C., Ethé, C., Cadule, P., Aumont, O., Salas y  
23 Mélia, D., Voltaire, A. and Madec, G.: Skill assessment of three earth system models with  
24 common marine biogeochemistry, *Clim. Dyn.*, 40(9–10), 2549–2573,  
25 <https://doi.org/10.1007/s00382-012-1362-8>, 2013.
- 26 Skákala, J., Bruggeman, J., Brewin, R. J. W., Ford, D. A. and Ciavatta, S.: Improved  
27 Representation of Underwater Light Field and Its Impact on Ecosystem Dynamics: A Study in  
28 the North Sea, *J. Geophys. Res. Oceans*, 125(7), <https://doi.org/10.1029/2020JC016122>,  
29 2020.
- 30 Sosik, H. M.: Characterizing seawater constituents from optical properties, *Real-Time Coast.*  
31 *Obs. Syst. Ecosyst. Dyn. Harmful Algal Blooms* Ed. Babin M Roesler CS Cullen JJ  
32 UNESCO, 281–329, 2008.
- 33 Steinacher, M., Joos, F., Frölicher, T. L., Bopp, L., Cadule, P., Cocco, V., Doney, S. C.,  
34 Gehlen, M., Lindsay, K., Moore, J. K., Schneider, B. and Segschneider, J.: Projected 21st  
35 century decrease in marine productivity: a multi-model analysis, *Biogeosciences*, 7(3), 979–  
36 1005, <https://doi.org/10.5194/bg-7-979-2010>, 2010.
- 37 Stow, C. A., Jolliff, J., McGillicuddy, D. J., Doney, S. C., Allen, J. I., Friedrichs, M. A. M.,  
38 Rose, K. A. and Wallhead, P.: Skill assessment for coupled biological/physical models of  
39 marine systems, *J. Mar. Syst.*, 76(1–2), 4–15, <https://doi.org/10.1016/j.jmarsys.2008.03.011>,  
40 2009.



- 1 Stramma, L., Johnson, G. C., Sprintall, J. and Mohrholz, V.: Expanding Oxygen-Minimum  
2 Zones in the Tropical Oceans, *Science*, 320(5876), 655–658,  
3 <https://doi.org/10.1126/science.1153847>, 2008.
- 4 Tagliabue, A., Bopp, L., Dutay, J.-C., Bowie, A. R., Chever, F., Jean-Baptiste, P., Bucciarelli,  
5 E., Lannuzel, D., Remenyi, T., Sarthou, G., Aumont, O., Gehlen, M. and Jeandel, C.:  
6 Hydrothermal contribution to the oceanic dissolved iron inventory, *Nat. Geosci.*, 3(4), 252–  
7 256, <https://doi.org/10.1038/ngeo818>, 2010.
- 8 Taylor, K. E.: Summarizing multiple aspects of model performance in a single diagram, *J.*  
9 *Geophys. Res. Atmospheres*, 106(D7), 7183–7192, <https://doi.org/10.1029/2000JD900719>,  
10 2001.
- 11 Teruzzi, A., Dobricic, S., Solidoro, C. and Cossarini, G.: A 3-D variational assimilation  
12 scheme in coupled transport-biogeochemical models: Forecast of Mediterranean  
13 biogeochemical properties: 3D-VAR IN BIOGEOCHEMICAL MODELS, *J. Geophys. Res.*  
14 *Oceans*, 119(1), 200–217, <https://doi.org/10.1002/2013JC009277>, 2014.
- 15 Terzić, E., Lazzari, P., Organelli, E., Solidoro, C., Salon, S., D’Ortenzio, F. and Conan, P.:  
16 Merging bio-optical data from Biogeochemical-Argo floats and models in marine  
17 biogeochemistry, *Biogeosciences*, 16(12), 2527–2542, [https://doi.org/10.5194/bg-16-2527-](https://doi.org/10.5194/bg-16-2527-2019)  
18 2019, 2019.
- 19 Thierry, V. and Bittig, H.: Argo quality control manual for dissolved oxygen concentration,  
20 2018.
- 21 Thierry, V., Bittig, H., Gilbert, D., Kobayashi, T., Kanako, S. and Schmid, C.: Processing  
22 Argo oxygen data at the DAC level, Ifremer., 2018.
- 23 Tuan Pham, D., Verron, J. and Christine Roubaud, M.: A singular evolutive extended Kalman  
24 filter for data assimilation in oceanography, *J. Mar. Syst.*, 16(3–4), 323–340,  
25 [https://doi.org/10.1016/S0924-7963\(97\)00109-7](https://doi.org/10.1016/S0924-7963(97)00109-7), 1998.
- 26 Vichi, M., Lovato, T., Lazzari, P., Cossarini, G., Gutierrez, E., Mattia, G., Masina, S.,  
27 McKiver, W. J., Pinardi, N. and Solidoro, C.: The Biogeochemical Flux Model (BFM):  
28 Equation Description and User Manual, BFM version 5.1, BFM Report series N. 1, Release  
29 1.1, July 2015, Bologna, Italy, 104pp., 2015.
- 30 Wanninkhof, R.: Relationship between wind speed and gas exchange over the ocean revisited:  
31 Gas exchange and wind speed over the ocean, *Limnol. Oceanogr. Methods*, 12(6), 351–362,  
32 <https://doi.org/10.4319/lom.2014.12.351>, 2014.
- 33 Ward, B. A., Friedrichs, M. A. M., Anderson, T. R. and Oschlies, A.: Parameter optimisation  
34 techniques and the problem of underdetermination in marine biogeochemical models, *J. Mar.*  
35 *Syst.*, 81(1–2), 34–43, <https://doi.org/10.1016/j.jmarsys.2009.12.005>, 2010.
- 36 Williams, R. G. and Follows, M. J.: Ocean dynamics and the carbon cycle: Principles and  
37 mechanisms, Cambridge University Press., 2011.
- 38 Wong, Keeley, Robert, Carval, Thierry and Argo Data Management Team,: Argo Quality  
39 Control Manual for CTD and Trajectory Data, , <https://doi.org/10.13155/33951>, 2015.



- 1 Xing, X., Claustre, H., Blain, S., D'Ortenzio, F., Antoine, D., Ras, J. and Guinet, C.:
- 2 Quenching correction for in vivo chlorophyll fluorescence acquired by autonomous platforms:
- 3 A case study with instrumented elephant seals in the Kerguelen region (Southern Ocean):
- 4 Quenching correction for chlorophyll fluorescence, *Limnol. Oceanogr. Methods*, 10(7), 483–
- 5 495, <https://doi.org/10.4319/lom.2012.10.483>, 2012.

6